Exploring Cooperative Effects with Nitrogen-Vacancy Centres in Diamond

By

Rochelle Martin

A thesis submitted to Macquarie University
for the degree of Master of Research
Department of Physics and Astronomy
February 2017

Examiner's Copy

Typeset in LaTeX 2_ε.

Except where acknowledged in the customary manner, the material presented in this thesis is, to the best of my knowledge, original and has not been submitted in whole or part for a degree in any university.

Rochelle Martin

Acknowledgments

This thesis would not have been possible without the guidance, support and friendship of so many. I would especially like to thank Thomas Volz, Gavin Brennen and Ben Baragiola. I have been so fortunate to have this team of knowledgeable, enthusiastic and, above all, endlessly-patient, supervisors. I am incredibly grateful for enormous amounts of time they spent guiding me on this journey from student to researcher.

I also thank Matt van Breugel, Mattias Johnsson and Carlo Bradac, who have been both friends and mentors throughout the year. They have always been willing to help in every way possible, and their kindness has not gone unnoticed nor unappreciated.

I have had the support of so many in this department, from our administration staff to our Head of Department Mike Steel, whose door has always been open to me. I would also like to thank Jo Dawson, our MRes Advisor, for her guidance throughout the year.

I would also like to acknowledge Mr Grant, my high school science teacher, whose most valuable lesson was that physics has the power to change the world. Your inspiration was a large part in my decision to study physics, so I hold you personally responsible for my current coffee addiction.

I wish to thank my friends, for the fond memories we share and the support I know I can always count on. I would like to thank my loving partner James, and his family who have been so very welcoming. James has been a constant presence through the year, and should probably quality for a Masters of Research through the vicarious journey he has consequently been subjected to. Above all, I wish to thank my parents, my three brothers and my one sister-in-law, who have always encouraged and believed in me. My friends and family have been by my side throughout this entire journey, and I cannot thank them enough for their ongoing love and support.

List of Publications

- C. Bradac, M. Johnsson, M. van Breugel, B. Baragiola, R. Martin, M. L. Juan, G. Brennen, and T. Volz, *Observation of room-temperature spontaneous superradiance from single diamond nanocrystals*, pp. 1-12 (2016) 1608.03119
  URL http://arxiv.org/abs/1608.03119

- R. Martin, B. Baragiola, M. Johnsson, T. Volz, and G. Brennen "Superradiance from nitrogen-vacancy centres in nanodiamonds", 2016 AIP Conference

- R. Martin, B. Baragiola, M. Johnsson, T. Volz, and G. Brennen "Exploring superradiance from nitrogen-vacancy centres in nanodiamonds", *In preparation*

Abstract

We present a theoretical study of superradiance with nitrogen-vacancy centres in nanodiamonds. Superradiance is a radiation phenomenon where identical proximal atoms emit photons collectively. A nitrogen-vacancy centre is an "artificial atom" in which indistinguishability cannot be assumed a priori. Nevertheless, superradiance from nitrogen-vacancy centres in nanodiamond has been observed very recently. While a phenomenological model built on Dicke states and the known properties of nitrogen-vacancy centres was able to explain the experimental findings well, many of the microscopic details that introduce distinguishability were not included: *(i)* photon emission into orientation-dependent superpositions of polarizations, *(ii)* transition and permanent dipole-dipole interactions, *(iii)* random distributions of transition frequencies and spatial locations, and *(iv)* nitrogen-vacancy centres couple to lattice vibrations. These effects are generally expected to diminish superradiance. In this thesis, we develop numerical simulations based on a model which takes these features into account. Our program can, in principle, perform simulations on the emission dynamics of up to 13 centres. Based on the results presented, we conclude that superradiance persists for certain nitrogen-vacancy centre densities, consistent with the experimental findings. Furthermore, our simulation tools provide a theoretical framework to study coherently driven dynamics, other temperature regimes, or use of other colour centres.

Contents

A kiss on the hand may be quite continental,
but diamonds are a girl's best friend.

Marilyn Monroe

1

Introduction

Humans have long been fascinated with diamond, initially due to its natural beauty but increasingly because of its technological relevance. Diamond has outstanding mechanical, thermal, electric and optical properties [1]. In more recent years, its usefulness in quantum engineering has emerged. Imperfections in the diamond structure can give rise to the formation of "artificial atoms", such as the nitrogen-vacancy (NV) centre, which occurs when two adjacent carbon atoms are replaced with a nitrogen atom and a vacancy. Many of the properties of the NV centre have been well studied due to its striking potential for a multitude of applications [2], ranging from quantum information [3] and metrology [4] to biology [5]. However, a well-known quantum optics phenomenon has remained elusive until very recently — cooperative behaviour among many NV centres in a single diamond resulting in superradiant behaviour [6]. Superradiance has been observed in a number of other systems but never in diamond; this is the first report of superradiance in a true nanoscale system equivalent to the one originally envisioned by Dicke [7]. Even more surprisingly, it was observed at room temperature. Given that superradiance relies on the formation of

highly entangled Dicke states, this observation is both surprising and striking. As the NV centre is far from being an ideal atom, a theoretical study taking proper account of many of the details of the system is justified and timely, especially in light of the many NV-based quantum technologies that have been proposed.

1.1 Superradiance

In 1954 Dicke considered n closely packed identical emitters coupled to the radiation field. When excited, the emitters radiate photons. In this configuration, it cannot be determined which photon came from which emitter. This gives rise to a characteristic burst of photon emission, with a peak emission rate proportional to n^2. This collective behaviour is termed *superradiance*. The emission is very different to the behaviour of n independent emitters, which decay exponentially and with emission rate intensity proportional to n. Superradiance requires that emitters are both spectrally and spatially indistinguishable. Given this spectral requirement, it is not surprising that the first observations of superradiance were from atomic gases [8]. Dicke's seminal proposal required emitters to be within a volume much smaller than the cube of the emission wavelength, which at the time was difficult to achieve experimentally. Instead, initial observations of superradiance relied on a pencil-shaped sample of gas molecules confined to distances much smaller than the emission wavelength in two dimensions, which resulted in superradiant bursts at the ends of the pencil [9].

The first experimental observation of strong superradiance was by Skribanowitz et al. in 1973 from room-temperature hydrogen-flouride gas at millitorr pressures [8]. Superradiance has since been observed in a variety of systems including from two trapped ions in 1996 [10], from quantum dots in 2007 [11] and from two superconducting qubits in 2014 [12]. The first experimental observation of superradiance from atom-type emitters confined to a volume much smaller than the cube of the emission wavelength, as originally envisioned by Dicke, was reported recently for NV centres in nanodiamonds [6].

An ensemble of n quantum emitters exhibiting superradiance was originally of interest as it is an exactly solvable quantum system which exhibits a phase transition between superradiant and normal behaviour [13–15]. In recent years, a superradiant laser source with

unprecedented narrow linewidth was realised [16] and cooperative emission has been used to achieve laser cooling below the recoil limit [17, 18]. Superradiance has been proposed to enhance long-distance quantum communication [19, 20], for realising quantum memories [21] and for single-photon generation [22, 23]. Outside the pure quantum-optics domain, superradiance has been predicted to occur in the vicinity of black holes [24, 25], and in light-harvesting complexes [26].

In solid-state systems, finite size effects can be eliminated by placing atoms (or artificial atoms) in structures such as cavities and waveguides, where preferential coupling to one spatial light mode is guaranteed by means of mode engineering [27–34]. Studying superradiance in solid-state systems is challenging due to the inhomogeneous broadenings and large dephasing rates involved. It should also be noted at this point that superradiance is regularly discussed in the context of excitonic semiconductor systems. Here we are concerned with "atomic" superradiance where the emitters are well separated and interact through the light field. In excitonic systems this is usually not true which makes them non-trivial [35].

As Dicke outlined in his seminal paper, while constructive interference effects can lead to superradiance, destructive interference can lead to the related phenomenon of subradiance [7]. Subradiance is characterized by decreased photon emission rates, resulting from partial trapping of light in a system [36, 37]. Subradiance has recently been observed experimentally in a large cloud of cold atoms [38, 39]. Subradiance has also been studied in the context of cavities [40] and waveguides [41].

The study of superradiance is also of interest as by time-reversal symmetry, superradiance must be accompanied by superabsorption, which is characterised by enhanced absorption rates. In most set-ups, superradiance is dominant, however it has been proposed that through suitable engineering, structures can be created with strong superabsorption [42]. This could result in novel photon detection and light-based power transmission technologies. Superabsorption follows the same theoretical framework as superradiance and hence the obvious questions to raise is whether NV centres in diamond could act as superabsorbers. However, such investigations are outside the scope of this thesis.

1.2 The nitrogen-vacancy centre

Starting from the time that nitrogen was first identified as a diamond impurity in 1959 by Kaiser and Bond [43], the NV centre has been at the focus of an intense and ongoing research effort. The NV centre is an extrinsic defect in the tetrahedral carbon lattice of diamond, in which a nitrogen atom is substituted by a carbon atom, and an adjacent carbon site is left vacant (Fig 3.1A). This atomic configuration yields a neutral NV^0 state and by accumulating an additional electron the more stable, negatively charged NV^- state is formed. From here on, the abbreviation 'NV' will refer specifically to the NV^- state. NV centres occur naturally in diamond, but they can also be artificially created by various methods [44–46]. Through artificial creation, diamonds can be engineered to meet a desired spatial location of NV centres [47, 48], or aligned to a preferred orientation [49–52].

The favourable optical and spin properties of NV centres make them a promising technology for a range of applications. Optically, they are interesting for quantum communication as single NV centres can act as a photostable single photon source because each NV centre has a finite re-excitation time between emitting photons [53]. The ground electronic state of the NV centre consists of a spin triplet with spin projection subspace $m_s = 0$ split from the degenerate $m_s = +1, -1$ subspace by zero field splitting ~ 2.88 GHz [54]. A qubit can be stored in the $m_s = 0, \pm 1$ states and coherently manipulated by microwave fields. NV centres are considered viable qubits since even at room temperature they exhibit relatively long coherence times of $T_1 = 6.0$ ms and $T_2 = 3.3$ ms [55, 56], during which they can be optically initialized, controlled and read out, as required by the DiVincenzo criteria for quantum computing [57]. Simple logic gates have been demonstrated at room-temperature [3, 58]. In terms of quantum metrology, NV centre spins can act as promising precision sensors as their energy levels are sensitive to in the presence of external fields, which can be detected using a combination of microwave and optical fields. In particular, NV centres have a range of applications in magnetometry [4, 58–60], electrometry [61] and thermometry [62]. Additionally, NV centres in nanodiamond are of interest for biological applications as they are bio-compatible [63]. They have the potential to be used as precision sensors in vivo [64, 65], and they can be used for biolabelling [5] and drug delivery [66].

Historically, NV centres have received the most attention. However, they are not the only diamond-defect of interest to the scientific community — silicon-vacancy (SiV) centres [67, 68] and germanium-vacancy (GeV) [69] centres potentially exhibit similar spin-optical properties. In particular, SiV centres have better optical properties than NV centres as they have less variance in the centre frequency and might therefore exhibit stronger superradiance. In addition, SiV and GeV centres have no permanent electric dipole moment (to first order) as they have an inversion symmetry. Thus, unlike the NV centre, they will be unaffected by the dipole-dipole interaction of permanent dipoles which hinder NV centre superradiance. Here we focus our attention on NV centres as this is the best-known defect system, and as reported by our group, the system in which superradiance was recently seen. However, given the structural similarities between the defect centres, the model developed here can readily be adjusted to describe SiV or GeV centres, and to predict the occurrence and strength of superradiance in these systems.

1.3 Superradiance from nitrogen-vacancy centres

Our research group recently reported the observation of superradiance from nanodiamonds with high densities of NV centres [6]. This study was inspired by an earlier independent experiment, also conducted by our group, where nanodiamonds with high densities of NV centres exhibited enhanced optical trapping [70]. In the superradiance study, fluorescence decay following pulsed laser excitation from 100 different nanodiamonds with high densities of NV centres was studied. Due to inhomogeneities in the nanodiamonds, not all NV centres act cooperatively. Collections of spectrally similar NV centres act cooperatively within small domains. Within these domains, NV centres were modelled following Dicke physics, with an additional phenomenological dephasing mechanism. This model will be referred to as the Bradac-Johnsson (BJ) model. Through comparison of fluorescence decay from this model with that in the experiment, an estimate was constructed of the maximal domain size in each nanodiamond. Many of the nanodiamonds exhibited behaviour that required domain sizes larger than one (indicating cooperative behaviour) to fit the experimental results [6]. Figure 1.1 shows the normalised fluorescence decay curves for 4 of the nanodiamonds studied.

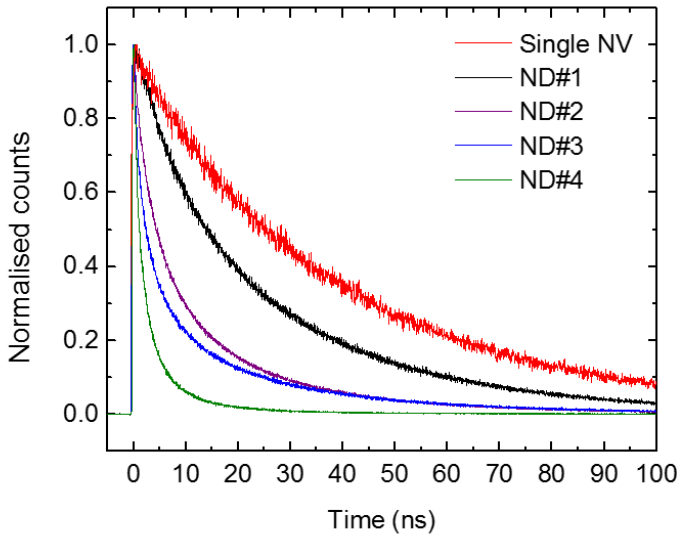

FIGURE 1.1: Measured rate of fluorescence decay over time for 5 nanodiamonds after they were excited by a 10ps laser pulse, normalised to the maximum of each curve. The faster decay rates corresponds to superradiant behaviour. [6]

Shortly after our paper was posted to the arXiv, a related study from the Lukin group at Harvard appeared in which they observed superradiance from two SiV centres which were optically coupled in a waveguide at low temperatures [71].

To date, the possible effects of superradiance on the aforementioned applications of NV centres has not been considered because most investigations have assumed low density regimes. However, in high-density samples, superradiance could play a striking role in enhancing the viability of some of these applications due to the coherence and higher peak intensity of the photons emitted.

1.4 In this thesis

In this thesis, we conduct a detailed theoretical study of superradiance from NV centres in nanodiamond. This is done as an extension to the BJ model, and also to study superradiance in the context of NV centres generally.

This has been achieved through the creation of a new model, which is numerically simulated in MATLAB. This new model is different from the BJ model in that the full density matrix is simulated, as opposed to just tracking the populations in the Dicke ladder. This

allows us to explicitly include the dipole-dipole terms and properly model dephasing. In addition, in this model we account for orientation effects and spatial inhomogeneities, and we extend the spectral inhomogeneity effects.

To set the scene and introduce the reader to the theoretical model, Chapter 2 gives a brief technical introduction to Dicke superradiance. In Chapter 3, we examine NV centres in nanodiamond to inform our model. We first explore a single NV centre, examining how its physical structure gives rise to a complex vibronic structure and the subsequent emission spectrum. We also consider how the orientation of an NV centre determines the superposition of the polarizations it can emit into. Secondly, we discuss ensembles of NV centres whereby dipole-dipole interactions and dephasing emerge. NV centres have both transition and permanent dipole moments which must both be considered. Finally, we consider NV centres with some degree of distinguishability, both spectrally and spatially. In Chapter 4, we describe both the BJ model and our new model. As I was most involved with creating the new model, this is the area in which most emphasis has been placed. In Chapter 5, we discuss the results of our work. We are able to confirm the accuracy of some aspects of the phenomenological BJ model, and we discuss the impact of effects not previously considered. In Chapter 6, we outline our key conclusions, and present possible directions for future work. Appendix A contains a discussion of the master equation that governs our simulation.

The most practical solution is a good theory.

Albert Einstein

2

Superradiance

Dicke superradiance is the cooperative emission of photons from identical proximal emitters. A detailed theoretical description of superradiance is found in Gross and Haroche's 1982 essay on the subject [9].

2.1 Superradiance for two spins

Consider two spin-1/2 systems. Each of these systems starts in its excited state $|e\rangle$, and it can spontaneously decay to its ground state $|g\rangle$. We can describe the total Hilbert space as the tensor product of the two individual Hilbert spaces, so that the possible states of the collection are $|ee\rangle$, $|eg\rangle$, $|ge\rangle$ and $|gg\rangle$. Superradiance is most clearly described by the coupled-spin basis. This basis is spanned by the symmetric states $|ee\rangle$, $(|eg\rangle + |ge\rangle)/\sqrt{2}$, and $|gg\rangle$, which have angular momentum $J = 1$, and the antisymmetric state $(|eg\rangle - |ge\rangle)/\sqrt{2}$ which has angular momentum $J = 0$. In this basis, the states can thus be labelled $|J, M\rangle$, where $M \in \{J, ... - J\}$ is the spin projection. In this $|J, M\rangle$ basis we thus have $|1, 1\rangle = |ee\rangle$, $|1, 0\rangle = (|eg\rangle + |ge\rangle)/\sqrt{2}$, $|1, -1\rangle = |gg\rangle$ and $|0, 0\rangle = (|eg\rangle - |ge\rangle)/\sqrt{2}$.

In the case of independent emitters, both two-level systems will independently undergo exponential decay. However, if they act collectively, they instead act as a spin $J = 1$ system. They start in the $|1, 1\rangle$ state, before decaying through the $|1, 0\rangle$ state to the $|1, -1\rangle$ state. Even with two spins, the emission from the collectively acting ensemble is different to that for independent emitters, as in Figure 2.1.

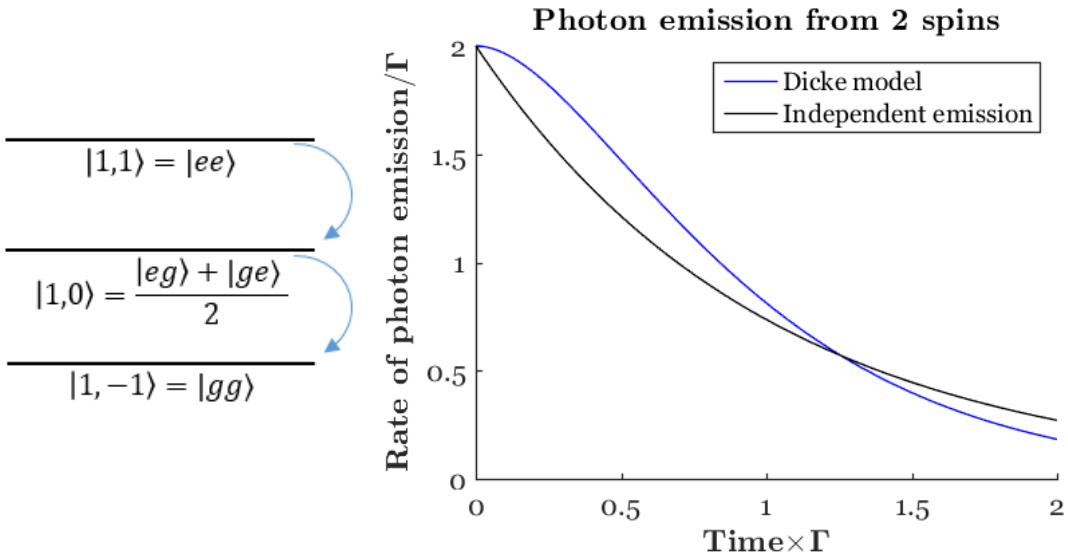

Figure 2.1: Left: the Dicke ladder for a two spin system. Right: Rate of photon emission from two spins, starting in the fully excited state.

2.2 Superradiance for n spins

For a larger number of systems, the result is analogous — n spin 1/2 systems behave as a spin $J = n/2$ system — termed the Dicke ladder. The Clebsch-Gordan coefficients can be used to express the Dicke states in terms of the product basis as

$$|J, M\rangle = \sqrt{\frac{(M+J)!(J-M)!}{(2J)!}} \sum_{\pi} |\underbrace{g \dots g}_{J-M} \underbrace{e \dots e}_{J+M}\rangle \tag{2.1}$$

The normalisation factor is found from the combinatorial problem *'from $n = 2J$ spin-1/2 systems, choose $(J + M)$ to be excited'* and π denotes the sum over all permutations with $J + M$ excited atoms.

The raising and lowering operators for the ith two-level system are $\hat{s}_i^+ = |e\rangle \langle g|_i$ and $\hat{s}_i^- =$

$|g\rangle \langle e|_i$, respectively. To describe collective behaviour, the collective raising and lowering operators are $\hat{S}^{\pm} = \sum_{i=1}^{n} \hat{s}_i^{\pm}$. The rate of collective decay from Dicke state $|J, M\rangle$ is

$$\Gamma \langle J, M| \hat{S}^{+}\hat{S}^{-} |J, M\rangle = \Gamma(J + M)(J - M + 1). \tag{2.2}$$

At the top and bottom of the ladder, i.e. for the $|J, J\rangle \rightarrow |J, J-1\rangle$ and $|J, -J+1\rangle \rightarrow |J, -J\rangle$ transitions, the rate of collective decay is $\Gamma 2J = \Gamma n$, while halfway down the ladder, for the $|J, 1\rangle \rightarrow |J, 0\rangle$ and $|J, 0\rangle \rightarrow |J, -1\rangle$ transitions, the rate of collective decay is $\Gamma J(J + 1) \approx \Gamma n^2/4$. This explains the shape of the photon emission from a collectively acting sample — as the collection of systems cascades down the Dicke ladder, the florescence increases, peaks with an intensity that scales with n^2 at halfway down the ladder, then decreases, as in Fig. 2.2. This behaviour can be described with the superradiance master equation [6]

$$\frac{d\hat{\rho}}{dt} = -\frac{\Gamma}{2}\mathcal{D}[\hat{\rho}] = -\frac{\Gamma}{2}\left(\hat{S}^{+}\hat{S}^{-}\hat{\rho} + \hat{\rho}\hat{S}^{+}\hat{S}^{-} - 2\hat{S}^{-}\hat{\rho}\hat{S}^{+}\right). \tag{2.3}$$

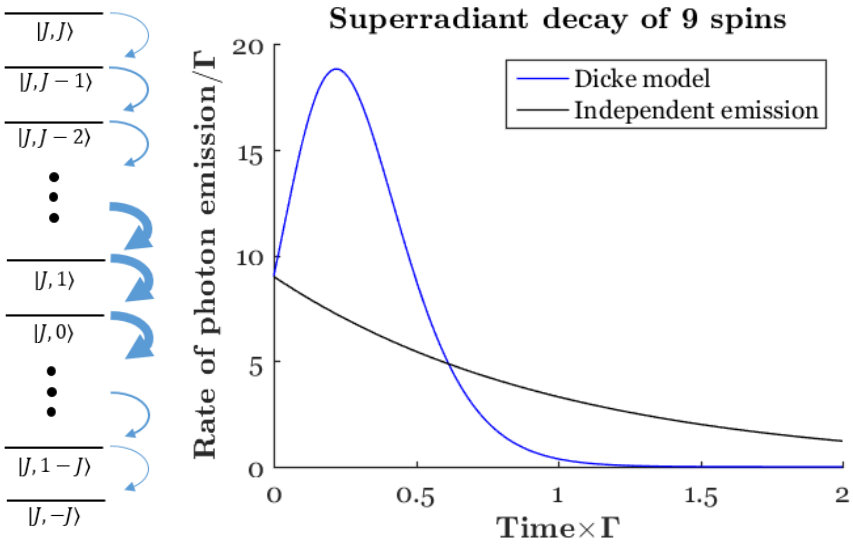

FIGURE 2.2: Left: Dicke ladder, where the blue lines indicate optical transitions. The thickness of the line corresponds to the intensity of the transition. Right: Dicke superradiance as compared to independent decay.

Truth ... is much too complicated to allow anything but approximations.

John von Neumann

3

Nitrogen-vacancy centres in diamond

In order to model superradiance from NV centres, we must first explore the physics of the NV centre itself. In Section 3.1, we explore how the physical structure of a single NV centre gives rise to its energy level structure. In Section 3.2 we consider multiple orientations as an additional consequence of this physical structure. In Section 3.3 we discuss ensembles of NV centres, and introduce dipole-dipole interactions and dephasing. In Section 3.4 we relax the restraint of identical emitters — both spectrally and spatially. Taking into account all of these effects we will then be ready to move on to the next chapter and craft our model of NV centre superradiance.

3.1 Energy level structure of an NV centre

As NV centres are fixed within the lattice, they do not possess any translational or rotational degrees of freedom. The NV complex can vibrate however, both in a molecular vibration but also as a whole coupling to lattice phonons. In addition, there is an orbital degree of freedom, as the electrons can take different configurations, resulting in a rich vibrational and electronic (vibronic) energy structure.

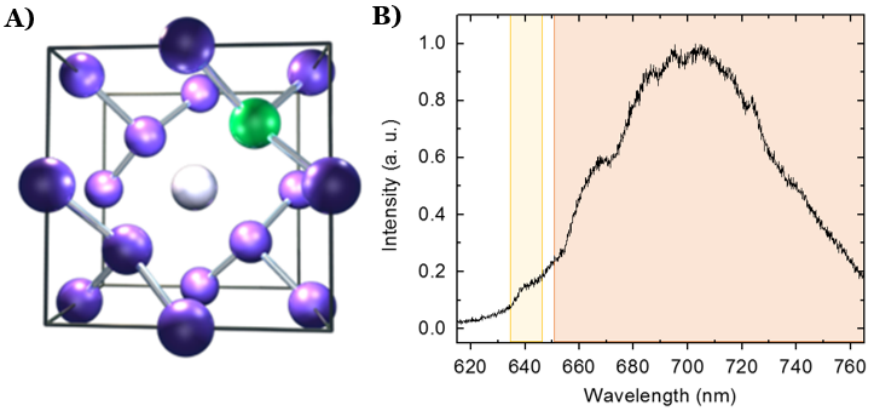

FIGURE 3.1: A) Diamond structure with a single NV centre where purple, green and white represent carbon atoms, nitrogen atoms, and vacancies, respectively. B) Typical fluorescence spectrum of an NV centre in a nanodiamond at room temperature. The yellow region indicates the location of the ZPL and the orange region indicates the vibrational sideband. [6]

In an NV centre the nitrogen atom is bonded to three carbon atoms and has a dangling bond in the direction of the vacancy (Fig. 3.1A). This structure gives the NV centre three-fold rotational symmetry and three planes of vertical symmetry, described by the group C_{3v}. Allowable operations in the C_{3v} symmetry group are the identity, rotations by $2\pi/3$ and $4\pi/3$, and reflection through any of the three symmetry planes, denoted as E, C_3, C_3^2, σ_1, σ_2, and σ_3, respectively. Representations are sets of matrices which follow the same product rules as elements in the group. The C_{3v} group has three irreducible representations (irreps), which are named according to their dimensionality. The one dimensional irreps are called A_1 and A_2, and the two dimensional irrep is called E. As the operations preserve the symmetry of the centre, they must commute with the molecular Hamiltonian. Each irreducible representation corresponds to a single electron orbital, which is labelled with the equivalent lowercase letter. The dimension of the representation gives the degeneracy of the orbital, so an NV centre must have two a orbitals, denoted a_1' and a_1, and two degenerate e orbitals as in Figure 3.2A [72, 73]. The NV centre has six electrons to place in these orbitals, which can hold two electrons each. The lowest energy configuration is $a_1'^2 a_1^2 e^2$, which corresponds to the triplet state $^3A_2$ and the singlet states ^1E and $^1A_1$. The next lowest energy configuration is $a_1'^2 a_1 e^3$ which corresponds to the triplet state ^3E as in Figure 3.2B [2, 74–77]. The triplet states have spin projection 0 ($m_s = 0$) and spin projection 1 ($m_s = \pm 1$) fine structure levels. From the Clebsh-Gordon coefficients of the C_{3v} group it

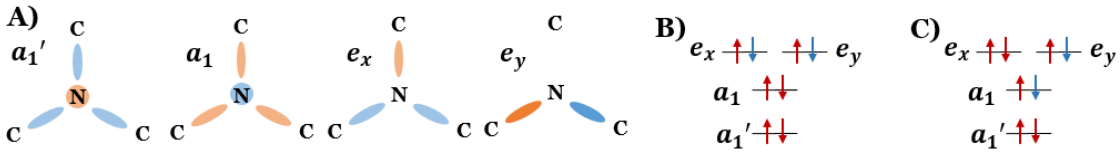

Figure 3.2: A) Single electron orbitals of NV. Distribution of electron density is represented by coloured lobes, with colour indicating phase. Based on figure from [76]. B) and C) represent the electron (red) hole (blue) structure of $a_1'^2 a_1^2 e^2$ and $a_1'^2 a_1^1 e^3$ respectively.

can be deduced that only spin-projection conserving transitions are optically allowed in NV centres [2, 74–76].

This group-theoretic description of a six-electron model has been confirmed by experimental studies. These studies confirm the level ordering and determine the optical and microwave transition frequencies between the levels. The $m_s = \pm 1$ excited-state fine-structure levels collapse to a single level at room temperature. At low temperature, phonon transition rates between these levels are slow compared to the decay rates, giving distinct energy levels. At room temperature, the phonon transition rates dominate over the decay rates, such that the 3-levels mix equally, as indicated in Figure 3.3 [78].

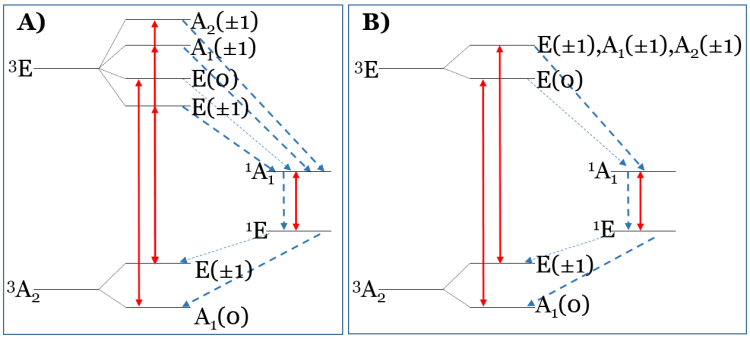

Figure 3.3: Diagram of the energy level structure of ^{1}4NV at A) low and B) room temperatures. The triplet levels are shown on the left, and the singlet levels on the right. Optical transitions are indicated with solid red arrows, and non-radiative transitions are indicated with dashed blue arrows. As there are no optical transitions between the triplet levels and the singlet levels, the singlet levels are termed 'dark' states, or the intersystem crossing (ISC) levels. Based on figures in [74], [75], [2] and [76]. Where there are discrepancies, Doherty's review paper has been upheld [2].

There is a fluorescent $^3E \rightarrow {}^3A_2$ transition which occurs at 637 nm for NV centres in bulk diamond [79], but may vary considerably in nanodiamonds due to strain and boundary conditions. This purely optical transition is called the zero phonon line (ZPL). However, the NV complex can vibrate giving rise to additional transitions involving phonon emission.

Transitions from a vibrational ground state of the excited electronic manifold can go to many possible vibrational levels within the ground electronic manifold. The probability of a transition ending up in any particular vibrational level is determined by the Frank-Condon overlap between the initial and final states. For NV centres at room temperature only around 3-5% of the photons are emitted into the ZPL (Figure 3.1B). For superradiance to occur, it must be impossible for the system to determine which photon has come from which emitter. If the emission of a photon is accompanied by the emission of a local phonon, that would suggest that it the origin of a photon could, in principle, be distinguished. However, these local phonons disperse into global phonons within picoseconds [80], erasing information about which NV centre emitted the phonon. Due to this erasure, we discard the vibrational substructure.

Dicke's model of superradiance is based on identical 2-level systems which, due to symmetry, can be treated in the collective angular momentum space. The BJ model was based very closely on the Dicke model, so the 6 NV levels were treated as a 2-level system, with an additional spin label. As the system is excited once and then allowed to decay, it does not matter which spin ground state the NV centre ends up in, so it can be treated as maintaining its spin. The dark states were included separately as a possible path of decay. In this way, each NV centre is either a spin projection-0 or a spin projection-1 2-level system. Thus for each spin polarization, cooperatively acting NV centres form a Dicke ladder with an additional decay channel representing 'dark' decay.

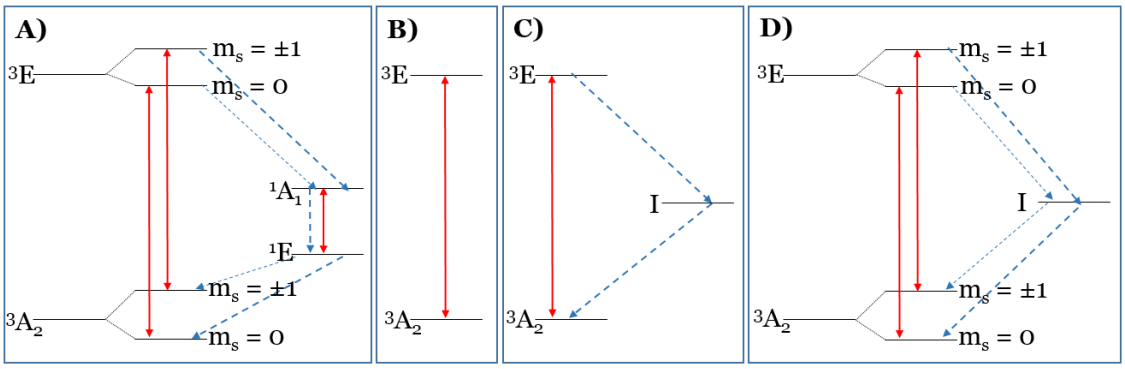

FIGURE 3.4: Electronic energy level diagrams for A) a real NV centre at room temperature B) a 2-level approximation of an NV C) a 3-level approximation of an NV and D) a 5-level approximation of an NV. Solid red lines denote optical transitions, and dashed blue lines indicate non-radiative transitions.

In our new model we wish to consider symmetry-breaking effects such as the dipole-dipole interactions. We thus cannot use the angular momentum space;we use instead the full tensor-product space. Thus we can describe each NV centre with as many levels as we choose. However the Hilbert space of n NV centres, modelled with m energy levels each, has dimension m^n, so the complexity of the computation scales rapidly. Thus, we choose three ways of approximating each NV centre — with 2, 3 and 5 levels, as shown in Figure 3.4. The 2-level approximation neglects the non-radiative ISC transitions, though it still captures the essential physics of superradiance. Without the singlet states, the $m_s = 0$ and $m_s = \pm 1$ populations are identical, so the approximation can be thought of as describing either one of the spin populations, or some arbitrary mixture of them. The 3-level approximation incorporates the effects of the intersystem crossing [81]. This third level, I, represents both the $^1A_1$ and ^1E singlet levels, as the systems decay quickly from $^1A_1$ to ^1E. The photons emitted are at 1042 nm [81], so they can be filtered out. The 3-level structure represents either an $m_s = 0$ or an $m_s = \pm 1$ population, as these have different rates of non-radiative decay. An NV centre which decays via I can change its spin, as requirement of spin conservation is only a property of optical transitions [82]. However, in the case of superradiance modelling, once an NV centre is in either of the ground levels, it is trapped so we do not need to treat the ground energy levels as distinct. When the system is continuously excited, as is the case for superabsorption, the spin of the ground states does matter. To track this, the 5-level approximation was used, which incorporates both spin populations. The decay rates used were, as given in Ref. [6], $^3E \rightarrow ^3 A_2$ with $2\pi \times 12.3$ MHz, $^3E(m_s = 1) \rightarrow I$ with $2\pi \times 9.4$ MHz and $^3E(m_s = 0) \rightarrow I$ with $2\pi \times 1.8$ MHz. The rates for non-optical decay out of the singlet states are more controversial — it is often thought that decay into the $m_s = \pm 1$ state is negligible compared to decay into the $m_s = 0$ state [83], however more recent work has shown the two rates to be similar [84], with the decay into the $m_s = 0$ state being about 1.2 times the decay into the $m_s = \pm 1$ state. We use this ratio, combined with the lifetime of the singlet states rates (371 ± 6) ns [84], to determine the rates from the singlet states to the $m_s = 0$ and $m_s = \pm 1$ ground states to be $2\pi \times 0.234$ MHz and $2\pi \times 0.195$ MHz, respectively.

3.2 Orientation of centres

The diamond lattice consists of two interpenetrating face-centred cubic (fcc) Bravais lattices, displaced along the body diagonal of the cubic cell by one quarter the length of the diagonal. It can be regarded as a face-centred cubic lattice with the two point primitive basis **0** and $(a/4)(\mathbf{x}+\mathbf{y}+\mathbf{z})$, a (0.356 nm, at 293 K) being the length of the conventional cubic cell. Every carbon atom is bonded to four carbon atoms, forming a tetrahedral structure (Fig. 3.5C) [1]. This restricts each NV centre to one of four possible orientations. As an NV centre is not invariant under a permutation of the nitrogen and the vacancy, the NV centre can point in one of two directions for each orientation, to give eight possible alignments. The four orientations are important when considering the polarization of light emitted, and the eight orientations are significant to the dipole-dipole interaction, as permutation of the nitrogen and the vacancy changes the direction of the permanent electric dipole.

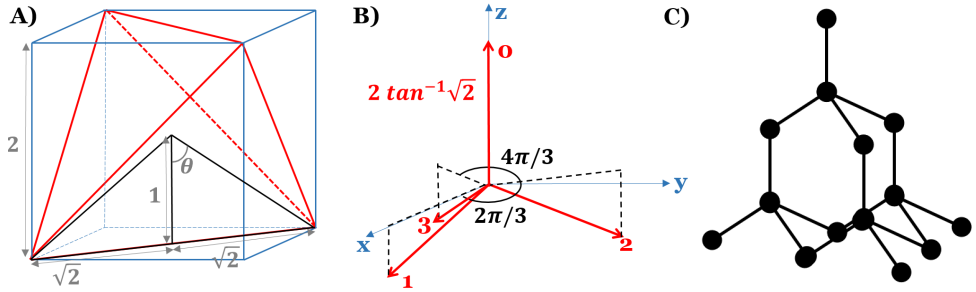

FIGURE 3.5: A) Construction of a tetrahedron (red) by connecting four non-adjacent vertices of a cube (blue) reveals the angle between orientations to be $2\tan^{-1}\sqrt{2} \approx 109.5^o$. B) Four orientations that an NV could take, indicating the Euler angles. C) The tetrahedral structure of diamond.

Without loss of generality, we fix one of the orientations along the z axis, chosen as our axis of quantization. In the spherical basis, with respect to the quantization axis, dipole transitions can decay into linearly polarized π photons with spin projection 0, and circularly polarized σ_+ and σ_- photons with spin projection ± 1. A change of spin via an optical transition must be accompanied by a photon of opposite spin. As NV centres forbid spin changing transitions, only π photons are emitted with respect to the NV centre's orientation. Photons must be in the same basis to be compared, so we choose the basis of the z axis orientation. The π photons emitted from other orientations can be converted to this basis via the Wigner D matrices [85]. For rotation operator $\mathcal{R}(\alpha, \beta, \gamma)$ the Wigner D matrices are

$D^j_{m',m}(\alpha,\beta,\gamma) \equiv \langle jm'|\mathcal{R}(\alpha,\beta,\gamma)|jm\rangle$. As we are concerned with spin conserving transitions which have been projected into other states, we have the initial state $|j,m\rangle = |1,0\rangle$, which maps to a superposition of $|j,m'\rangle = |1,-1\rangle$, $|j,m'\rangle = |1,0\rangle$ and $|j,m'\rangle = |1,1\rangle$. The rotation operator describes a rotation by the Euler angles α, β and γ about the z, y and z axes, respectively. Matrix ordering means that operations are performed from the right, so this is written $\mathcal{R}(\alpha,\beta,\gamma) = \mathcal{R}_z(\gamma)\mathcal{R}_y(\beta)\mathcal{R}_z(\alpha)$, where the rotation by α is performed first.

Orientation	α	β	γ
0	0	0	0
1	0	$2\tan^{-1}\sqrt{2}$	$\pi/3$
2	$2\pi/3$	$2\tan^{-1}\sqrt{2}$	$\pi/3$
3	$4\pi/3$	$2\tan^{-1}\sqrt{2}$	$\pi/3$

The application of these coefficients in the Wigner D matrices gives the coefficients for the transformation of the basis vectors [86]

$$\begin{aligned}
&\text{Orientation 0: } \bar{e}_0^* \to \bar{e}_0^* \\
&\text{Orientation 1: } \bar{e}_0^* \to -\frac{2}{3}\bar{e}_-^* - \frac{1}{3}\bar{e}_0^* + \frac{2}{3}\bar{e}_+^* \\
&\text{Orientation 2: } \bar{e}_0^* \to \left(\frac{1}{3} + \frac{i}{\sqrt{3}}\right)\bar{e}_-^* - \frac{1}{3}\bar{e}_0^* + \left(-\frac{1}{3} + \frac{i}{\sqrt{3}}\right)\bar{e}_+^* \\
&\text{Orientation 3: } \bar{e}_0^* \to \left(\frac{1}{3} - \frac{i}{\sqrt{3}}\right)\bar{e}_-^* - \frac{1}{3}\bar{e}_0^* - \left(\frac{1}{3} + \frac{i}{\sqrt{3}}\right)\bar{e}_+^*
\end{aligned} \tag{3.1}$$

As these polarizations are distinguishable, the NV centres only act collectively for photons emitted into the same polarization. Thus separate collective operators are required for each polarization. In the experiments our group conducted, no filtering of polarization was done, so the photons emitted from each polarization are incoherently summed. $P(\sigma|i)$ gives the proportion of the photon emitted from the i^{th} NV centre which is σ polarized. An NV in orientation 0 emits a photon into the π polarisation ($P(\pi|i) = 1$, $P(\sigma_\pm|i) = 0$). An NV in another orientation emits a photon into a superposition of the polarizations, with weightings $P(\pi|i) = 1/9$ and $P(\sigma_\pm|i) = 4/9$.

3.3 A collection of NV centres

We have previously discussed the behaviour of a single NV centre. In the case of an ensemble of NV centres, the dipole-dipole interactions and dephasing must also be considered.

3.3.1 Dipole-dipole interactions

The part of the Hamiltonian describing the energy of the interaction of the i^{th} dipole with the external electric field at its position is $\hat{H}_{\text{int}} = -\hat{\mathbf{d}}^{(i)} \cdot \hat{\mathbf{E}}(\mathbf{r}_i)$. The configuration of the molecular orbitals in the ^3E energy level of an NV centre gives rise to a permanent electric dipole $\hat{\mathbf{d}}^{(i)}_{\text{per}} = \mathbf{d}^{(i)}_{\text{per}} |e\rangle \langle e|^{(i)}$, where the permanent electric dipole vector $\mathbf{d}^{(i)}_{\text{per}} = d_{\text{per}} \boldsymbol{\varepsilon}^{(i)}$ has magnitude $d_{\text{per}} = 3.976 \times 10^{-30}$ C m and is aligned with the vertical axis of the NV centre, as described by the unit vector $\boldsymbol{\varepsilon}^{(i)}$ [87, 88]. The $^3A_2$ energy level also has a permanent electric dipole of magnitude 1.126×10^{-34} C m [89], however this will be neglected as it is negligible in comparison. NV centres can also have an induced dipole moment $\hat{\mathbf{d}}^{(i)}_{eg}$ which describes the transition between ^3E and $^3A_2$. As the diagonal components of the dipole operator describe the permanent dipole, the off diagonal elements describe the transition dipole. We thus have $\hat{\mathbf{d}}^{(i)}_{eg} = \mathbf{d}^{(i)}_{eg} (|e\rangle \langle g| + |g\rangle \langle e|)$. As the induced dipole moment also lies on the vertical axis of the NV centre, we can write $\mathbf{d}^{(i)}_{eg} = d_{eg} \boldsymbol{\varepsilon}^{(i)}$. The magnitude of d_{eg} can be calculated from the optical decay rate as $d_{eg} = \sqrt{\frac{3\pi\epsilon_0\hbar\Gamma_{\text{ZPL}}}{n_D k_0^3}}$. This is similar to the expression in the Gross and Haroche review paper [9], with the important distinction that as this is in a solid material, where k_0 is the wavenumber in vacuum, the density of states calculation introduces a factor of n_D, the index of refraction of diamond. $\Gamma_{\text{ZPL}} = 0.03\Gamma_{\text{tot}}$ is used as the transition dipole moment and describes the purely optical transition. As the transition dipole moment is a property of the NV centre, not its environment, the bulk decay rates are used. However, the precise rate depends on the way that interactions are mediated. If interactions are electrically mediated, as is the case with dipoles interacting with the surrounding electric field, $\Gamma_{\text{ZPL,vac}}$ is appropriate. In contrast, if the interactions are photon mediated, as for the transitional-dipole-transitional-dipole interaction, the appropriate rate is $\Gamma_{\text{ZPL,bulk}} = n_D \Gamma_{\text{ZPL,vac}}$ [90]. For notational purposes, the electronically mediated transitional dipole magnitude will be denoted d_{eg}, while the optically mediated transitional dipole magnitude will be relegated to $d'_{eg} = \sqrt{n_D} d_{eg}$. Taking $\Gamma_{\text{tot}} = 2\pi \times 12.3$ MHz [83] thus gives $d_{eg} = 2.980^{-30}$ C m. These two terms give the total dipole operator $\hat{\mathbf{d}}^{(i)} = \hat{\mathbf{d}}^{(i)}_{\text{per}} + \hat{\mathbf{d}}^{(i)}_{eg}$.

The kth mode of the electric field at point $\mathbf{r}_i$ will consist of *(i)* the vacuum field $\hat{\mathbf{E}}^{(k)}_{\text{vac}}(\mathbf{r}_i)$, *(ii)* the (classical) laser field $\mathbf{E}^{(k)}_{\text{laser}}(\mathbf{r}_i, t)$ (both discussed in Appendix A) and *(iii)* the electric

field of surrounding dipoles and charges. This laser field is not present for superradiance, but we can include it to study coherent dynamics. The electric field from the permanent dipoles $\hat{\mathbf{d}}^{(j)}_{\text{per}}$ of the surrounding NV centres is

$$\hat{\mathbf{E}}_{\text{per}}(\mathbf{r}_i) = \sum_{j\neq i} \frac{1}{4\pi\epsilon_0} \frac{3(\hat{\mathbf{d}}^{(j)}_{\text{per}} \cdot \mathbf{n}_{ij})\mathbf{n}_{ij} - \hat{\mathbf{d}}^{(j)}_{\text{per}}}{|\mathbf{r}_{ij}|^3} \tag{3.2}$$

where $\mathbf{r}_{ij} \equiv \mathbf{r}_i - \mathbf{r}_j$ and $\mathbf{n}_{ij} \equiv \mathbf{r}_{ij}/|\mathbf{r}_{ij}|$. As the electric field from surrounding charges is static, this will cause permanent shifts in the energy levels of the nearby NV centres and hence in their emission frequencies. This is accounted for by considering spectrally identical domains. The interaction of the dipoles of the i^{th} NV centre with the surrounding fields is therefore

$$\begin{aligned}\hat{H}^{(i)}_{\text{int}} = &- \hat{\mathbf{d}}^{(i)}_{\text{per}} \cdot \hat{\mathbf{E}}^{(k)}_{\text{vac}}(\mathbf{r}_i) - \hat{\mathbf{d}}^{(i)}_{\text{per}} \cdot \mathbf{E}^{(k)}_{\text{laser}}(\mathbf{r}_i, t) - \hat{\mathbf{d}}^{(i)}_{\text{per}} \cdot \sum_{j\neq i} \hat{\mathbf{E}}^{(j)}_{\text{per}}(\mathbf{r}_i) \\ &- \hat{\mathbf{d}}^{(i)}_{eg} \cdot \hat{\mathbf{E}}^{(k)}_{\text{vac}}(\mathbf{r}_i) - \hat{\mathbf{d}}^{(i)}_{eg} \cdot \mathbf{E}^{(k)}_{\text{laser}}(\mathbf{r}_i, t) - \hat{\mathbf{d}}^{(i)}_{eg} \cdot \sum_{j\neq i} \hat{\mathbf{E}}^{(j)}_{\text{per}}(\mathbf{r}_i)\end{aligned} \tag{3.3}$$

The first and second terms describe the interaction of the i^{th} permanent dipole with the electric vacuum field and electric laser field respectively. As detailed in Appendix A, these terms disappear under the rotating wave approximation. The third term describes the interaction of the i^{th} permanent dipole with the electric field created by the rest of the permanent dipoles.

$$\hat{H}^{(i)}_{\text{per-per}} = -\hat{\mathbf{d}}^{(i)}_{\text{per}} \cdot \sum_{j\neq i} \hat{\mathbf{E}}^{(j)}_{\text{per}}(\mathbf{r}_i) = \frac{d^2_{\text{per}}}{4\pi\epsilon_0} \sum_{j\neq i} \frac{\boldsymbol{\varepsilon}^{(i)} \cdot \boldsymbol{\varepsilon}^{(j)} - 3(\boldsymbol{\varepsilon}^{(i)} \cdot \mathbf{n}_{ij})(\boldsymbol{\varepsilon}^{(j)} \cdot \mathbf{n}_{ij})}{|\mathbf{r}_{ij}|^3} |e\rangle \langle e|^{(i)} \otimes |e\rangle \langle e|^{(j)} \tag{3.4}$$

The fourth term gives the interaction of the transition dipole with the surrounding vacuum field. In the typical master equation treatment, this gives rise to a term with a real part, which represent the conversion of excitations in the system to photons in the environment and is described with a Lindblad decay term, and an imaginary part, which represents a photon-mediated energy exchange between dipoles [9, 42, 91]. The induced electric field term is

$$\mathbf{E}^{(j)}_{eg}(\mathbf{r}_i) = \frac{1}{4\pi\epsilon_0 n_D^3} \frac{3(\mathbf{d}^{(j)}_{eg} \cdot \mathbf{n}_{ij})\mathbf{n}_{ij} - \mathbf{d}^{(j)}_{eg}}{|\mathbf{r}_{ij}|^3} \tag{3.5}$$

with the additional factor of n_D^3 arising as this is a photon-mediated process. Recalling that

the magnitude for the transition dipole moment is $d'_{eg} = \sqrt{n_D} d_{eg}$, we get

$$\begin{aligned}\hat{H}^{(i)}_{\mathrm{dd}} &= -\hat{\mathbf{d}}^{(i)}_{eg} \cdot \sum_{j \neq i} \hat{\mathbf{E}}^{(j)}_{eg}(\mathbf{r}_i) \\ &= \frac{d^2_{eg}}{4\pi\epsilon_0 n_d^2} \sum_{j \neq i} \frac{\boldsymbol{\varepsilon}^{(i)} \cdot \boldsymbol{\varepsilon}^{(j)} - 3(\boldsymbol{\varepsilon}^{(i)} \cdot \mathbf{n}_{ij})(\boldsymbol{\varepsilon}^{(j)} \cdot \mathbf{n}_{ij})}{|\mathbf{r}_{ij}|^3} \left(\hat{s}^{(i)}_+ \otimes \hat{s}^{(j)}_- + \hat{s}^{(j)}_+ \otimes \hat{s}^{(i)}_- \right)\end{aligned} \tag{3.6}$$

The rotating wave approximation has been made to get rid of non-energy conserving terms, as discussed in Appendix A. The fifth term describes the interaction of the transition dipole with the laser, which is detailed in Appendix A. The sixth term describes the interaction of a transition dipole with the electric field of the permanent dipoles and, similarly to the first and second terms, vanishes under the rotating wave approximation.

Considering the dipole-dipole interactions in further detail, assuming a separation of $r_0 = 7$ nm (as is typical of our nanodiamonds), we can compute the energy of a pairwise interaction of parallel dipoles which are perpendicular to the vector separating them. Expressing the energy as a frequency, $E = \hbar\Omega$, we get $\Omega_{\mathrm{dd}} = \frac{d^2_{eg}}{4\pi\epsilon_0 n_d^2 r_0^3 \hbar} = 2\pi \times 59.9$ MHz and $\Omega_{\text{per-per}} = \frac{d^2_{\mathrm{per}}}{4\pi\epsilon_0 r_0^3 \hbar} = 2\pi \times 625$ MHz. These strengths are consistent with Ref. [92], with the discrepancy arising from their use of a different bulk rate. As these terms both scale with r_0^3, it is clear that the permanent dipole term will always be much larger, as $\Omega_{\text{per-per}} : \Omega_{\mathrm{dd}} = d^2_{\mathrm{per}} : d^2_{eg}/n_D^2 \approx 10 : 1$.

3.3.2 Dephasing

Dephasing is a loss of coherence between spins, whereby the system recovers classical behaviour from a quantum system. It can be understood in Bloch sphere representation, in which the Bloch vector represents the collective state of the system. Decoherence corresponds to the accumulation of phases between individual spins, which results in the Bloch vector shrinking in the xy plane. As can be seen from Fig. 3.6, these phases are introduced by rotations around the z axis. In a tensor-product basis, dephasing equates to decreases in the off-diagonal terms in the density matrix. In NV centres in nanodiamonds, this is caused by different mechanisms based on interactions with the environment: charge traps, phonons and nearby spins. Dephasing can be either local, in which a local phase shift is caused by proximal effects, or global, in which all the centres are affected in an identical

way. For instance, molecular vibrations cause local dephasing, while long range phonons act globally. In the study of decay, global dephasing does not have any effect because while coherences between Dicke states decohere, populations in Dicke states do not change. However, when there is continuous laser driving, as is the case when studying superabsorption or trapping [93], global dephasing means that the system decoheres from the laser, so it will cause decoherence.

Since the BJ model looks at populations not coherences, only the diagonal elements of the density matrix are tracked. Therefore within this model, local dephasing could not be implemented in the usual way described above. As such, a phenomenological approach to dephasing was taken, as described in Section 4.1. The basic premise of this model is that dephasing results in a shrinking of the Block vector in the xy plane, which can be modelled as decreasing the number of NV centres that contribute to the collective spin.

In the present model, local dephasing is included through rotations in z, made via $\hat{s}_z$ operators. As dephasing is caused by an interaction of the system with the environment, the master equation treatment means that the dephasing is included through Lindblad terms with the jump operator $\hat{s}_z$.

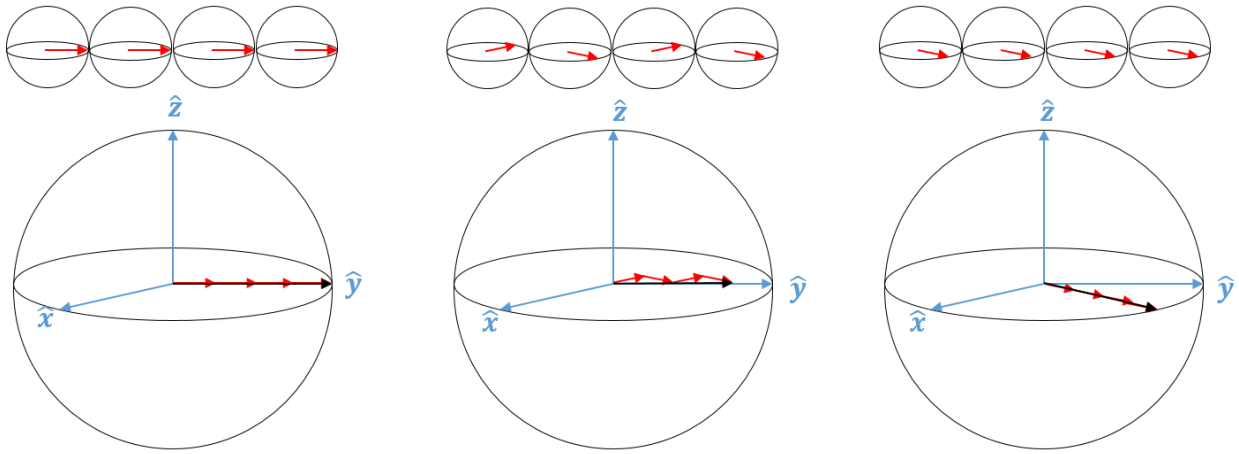

FIGURE 3.6: The individual spins (top) are added to give the Bloch vector for the collective systems. The left, middle and right images represent the initial state, local dephasing and global dephasing respectively. Note that in the central figure, the Block vector resulting from four locally dephasing spins could equally be composed of three spins with no dephasing. This gives rise to the dephasing treatment in the BJ model.

3.4 Distinguishability of NV centres

Dicke's original description of superradiance assumes perfectly indistinguishable emitters so close together in space that the location of photon emission cannot be determined. This indistinguishability is at the heart of the collective behaviour of the emitters. The photons emitted from NV centres in nanodiamond are not perfectly indistinguishable. First, NV centres are not spectrally identical, and second, they are not arbitrarily close together compared to the wavelength of radiation. However, there is strong experimental evidence that collective behaviour can persist for high-density NV nanodiamonds [6]. In this section, we determine the degree to which indistinguishability breaks down, due to both the spatial distribution of NV centres, and their spectral heterogeneity.

3.4.1 Spatial distinguishability

Dicke superradiance assumes that the separation between centres is much less than the wavelength of radiation, meaning that emitted photons cannot be distinguished from one another by their spatial phase. However, the experiments of our group at Macquarie University deal with nanodiamonds of size (110 ± 30) nm. NV centres have a ZPL of $\lambda = 639$ nm in vacuum, which translates to $\lambda' = \lambda/n_D = 264$ nm in the diamond material itself, where $n_D = 2.42$ is the diamond index of refraction. Thus Dicke's original assumption is not entirely valid for the ensemble of NV centres within a nanodiamond.

To determine if we need to consider the issue of spatial distinguishability, we first determine the plausibility of NV centres which are well separated in space having the same spatial phase. If spectral domains are likely to be localised in space, we don't need to consider the effect of spatial distinguishability as the spectral distinguishability will have already destroyed the collectivity.

The transition frequency of a centre is determined by its local environment. We can thus consider the transition frequency of an NV centre as a function of position in the diamond lattice. The Borsuk-Ulum theorem states that every continuous function from an n-sphere into Euclidean n-space maps some pair of antipodal points to the same point [94]. Thus, if we assume a background electric vector field or strain tensor field within the nanodiamond is

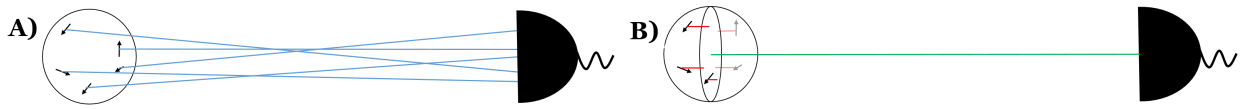

Figure 3.7: A: the total paths (blue) along which the spatial phase for NV centres is determined. B: Separation of these paths into contributions to a global phase (green) and a local phase (red).

differentiable, then for any spherical surface inside there must exist two antipodal points with the same field strength. Since it is the strength of these fields that determines the electronic structure of the NVs, this suggests that locations in the diamond with the same frequency need not be close together. Thus it is reasonable to consider domains of NV centres with the same frequency which are not physically co-located in the diamond.

In our new model, we determine a degree of distinguishability due to position. The time it takes a photon to travel from the NV centre to the detector a distance $\vec{r}$ away results in a phase $\exp(i\vec{k}' \cdot \vec{r})$, where $\vec{k}'$ is the wavevector which combines weighted portions of the wavevectors of the diamond, vacuum and optical elements. In the experimental setup, the emitted light is transmitted a long distance before being measured by the detector. As this distance is much greater than the width of the nanodiamond, the light from all NV centres can be approximated as travelling parallel, so the $\vec{k}$ vectors are all the same. Consider the plane through the centre of the nanodiamond perpendicular to $\vec{k}$. The phases can be broken into a global phase, which is acquired from the path between the plane and the detector, and a local phase, which depends on the distance vector $\vec{r}_\perp^{(i)}$ of the individual NV centre from the plane (Fig. 3.7). Note that a negative sign indicates centres on the detector side of the plane. The global phase can be neglected, and the local phase thus only involves travel through the nanodiamond, so $k' = n_D k$.

The state of one photon emitted from n excited NV centres into polarization σ and k-vector $\vec{k}$ is $\sum_{i=1}^{n} \hat{\sigma}_i \hat{a}_{\vec{k}}^\dagger D_\sigma^{(i)} |\text{vac}\rangle \otimes |\frac{n}{2}, \frac{n}{2}\rangle$, where $D^1_{\sigma,0}(\alpha_i, \beta_i, \gamma_i)$ has been abbreviated to $D_\sigma^{(i)}$. The state of one photon with normals $\vec{r}_\perp^{(i)}$ to the plane emitted from n excited NV centres into polarization σ and k-vector $\vec{k}$ is $\sum_{i=1}^{n} \hat{\sigma}_i^- \hat{a}_{\vec{k}}^\dagger D_\sigma^{(i)} \exp(i n_D \vec{k} \cdot \vec{r}_\perp^{(i)}) |\text{vac}\rangle \otimes |\frac{n}{2}, \frac{n}{2}\rangle$. The probability of detecting n indistinguishable photons can be calculated as the overlap of the states.

$$
\begin{aligned}
P(\text{Indist.}^{(\sigma)}) &= \left| \frac{\langle \text{vac}| \otimes \langle \tfrac{n}{2}, \tfrac{n}{2}| \left[\sum_{i=1}^{n} \hat{\sigma}_i^- \hat{a}_{\vec{k}}^\dagger D_\sigma^{(i)}\right]^\dagger \sum_{i'=1}^{n} \hat{\sigma}_{i'}^- \hat{a}_{\vec{k}}^\dagger D_\sigma^{(i')} \exp(in_D \vec{k} \cdot \vec{r}_\perp^{(i')}) \, |\text{vac}\rangle \otimes |\tfrac{n}{2}, \tfrac{n}{2}\rangle}{\langle \text{vac}| \otimes \langle \tfrac{n}{2}, \tfrac{n}{2}| \left[\sum_{i=1}^{n} \hat{\sigma}_i^- \hat{a}_{\vec{k}}^\dagger D_\sigma^{(i)}\right]^\dagger \sum_{i'=1}^{n} \hat{\sigma}_{i'}^- \hat{a}_{\vec{k}}^\dagger D_\sigma^{(i')} \, |\text{vac}\rangle \otimes |\tfrac{n}{2}, \tfrac{n}{2}\rangle} \right|^2 \\
&= \left| \frac{\langle \text{vac}| \, \hat{a}_{\vec{k}} \hat{a}_{\vec{k}}^\dagger \, |\text{vac}\rangle \otimes \langle \tfrac{n}{2}, \tfrac{n}{2}| \sum_{i=1}^{n} \hat{\sigma}_i^+ \hat{\sigma}_i^- D_\sigma^{*(i)} D_\sigma^{(i)} \exp(in_D \vec{k} \cdot \vec{r}_\perp^{(i)}) \, |\tfrac{n}{2}, \tfrac{n}{2}\rangle}{\langle \text{vac}| \, \hat{a}_{\vec{k}} \hat{a}_{\vec{k}}^\dagger \, |\text{vac}\rangle \otimes \langle \tfrac{n}{2}, \tfrac{n}{2}| \sum_{i=1}^{n} \hat{\sigma}_i^+ \hat{\sigma}_i^- D_\sigma^{*(i)} D_\sigma^{(i)} \, |\tfrac{n}{2}, \tfrac{n}{2}\rangle} \right|^2 \\
&= \left| \frac{\sum_{i=1}^{n} D_\sigma^{*(i)} D_\sigma^{(i)} \exp(in_D \vec{k} \cdot \vec{r}_\perp^{(i)})}{\sum_{i=1}^{n} D_\sigma^{*(i)} D_\sigma^{(i)}} \right|^2 \\
&= \frac{1}{(\sum_{i=1}^{n} D_\sigma^{i*} D_\sigma^{i})^2} \left(\left(\sum_{i=1}^{n} D_\sigma^{i*} D_\sigma^{i} \cos(n_D \vec{k} \cdot \vec{r}_\perp^{(i)}) \right)^2 + \left(\sum_{i=1}^{n} D_\sigma^{i*} D_\sigma^{i} \sin(n_D \vec{k} \cdot \vec{r}_\perp^{(i)}) \right)^2 \right)
\end{aligned}
\tag{3.7}
$$

Clearly if the local displacements are equal for each centre, the probability of indistinguishable photons is 1. If many centres are randomly distributed within a large region, the probability of indistinguishable photons becomes very small. Through periodic construction where $n_D \vec{k} \cdot \vec{r}_\perp^{(i)}$ goes to multiples of 2π, we can get collective effects even over large spatial displacements. However, if these displacements are too large, collectivity will start to break down due to the retardation time [95–98].

We thus have an expression for the fraction of decay that is indistinguishable at the detector, assuming all NV centres are excited. This can be used as an estimate of indistinguishability, regardless of the excitation of each NV centre. We use this expression as a weighting factor for the maximally indistinguishable part of decay. The remaining fraction is treated as undergoing completely distinguishable decay. This is only an estimate of the behaviour, as the amount of indistinguishability, given a general state, is quite complicated. However, it still provides some insight into how much indistinguishability we lose as a result of the spatial variance of the NV centres. From subsequent simulations of the system, we conclude that NVs which are spatially separated across the whole diamond can still act co-operatively, however the penalty imposed is that, for domain sizes of up to 10, only around 60 to 80% of their total photon emission will be collective.

We also consider the limiting behaviour in the case of large n. For large n, $D_\sigma^{i*} D_\sigma^{i} \approx 1/3$ (as for $\sigma = 0$, there is a $1/4$ chance of it being 1, and a $3/4$ chance of it being $1/9$, and for

$\sigma = \pm 1$, there is a 3/4 chance of being 4/9). Thus for large n, the above expression becomes

$$P(\text{Indist.}) = \frac{1}{n^2}\left(\left(\sum_{i=1}^{n}\cos(n_D\vec{k}\cdot\vec{r}_\perp^{(i)})\right)^2 + \left(\sum_{i=1}^{n}\sin(n_D\vec{k}\cdot\vec{r}_\perp^{(i)})\right)^2\right) \tag{3.8}$$

In addition, for a large number of spins the second term tends to zero as as $\sin(\theta)$ is an odd function and the $\theta_i = n_D\vec{k}\cdot\vec{r}_\perp^{(i)}$'s can be assumed to be symmetrically distributed. Thus for large n, the fraction of indistinguishability is simply the square of the mean of $\cos(\theta_i)$. To determine the mean of $\cos(\theta_i)$ we assume a sphere of radius $\theta_{\max} = n_D k r_D$ of randomly distributed NV centres, where r_D is the radius of the nanodiamond. Any given θ corresponds to a slice of this sphere. For large n, we can take the sum over the centres to be an integral over θ, where the probability of θ is illustrated in Figure 3.8.

$$\begin{aligned}
\text{Mean of } \cos(\theta_i) &= \int_{-\theta_{\max}}^{\theta_{\max}} (\text{probability of } \theta)\times\cos(\theta) \\
&= \int_{-\theta_{\max}}^{\theta_{\max}} \frac{\text{Volume of slice}}{\text{Volume of sphere}}\times\cos(\theta) \\
&= \int_{-\theta_{\max}}^{\theta_{\max}} \frac{\pi(\theta_{\max}^2-\theta^2)d\theta}{\frac{4}{3}\pi\theta_{\max}^3}\times\cos(\theta) \\
&= \frac{3\sin\theta_{\max}}{\theta_{\max}^3} - \frac{3\cos\theta_{\max}}{\theta_{\max}^2}
\end{aligned} \tag{3.9}$$

We thus have

$$P(\text{Indist.}) = \frac{9}{\theta_{\max}^4}\left(\frac{\sin^2\theta_{\max}}{\theta_{\max}^2} - \frac{2\sin\theta_{\max}\cos\theta_{\max}}{\theta_{\max}} + \cos^2\theta_{\max}\right). \tag{3.10}$$

It thus clear that configurations of many NV centres with a large spatial distribution have a quickly vanishing fraction of indistinguishability, with scaling like $1/\theta_{\max}^4$. Indistinguishability is clearly maximal for an infinitely small spatial distribution. As $\theta_{\max}$ increases, the indistinguishably quickly vanishes, going to zero at $\theta_{\max} \approx 4.49$. If $\theta_{\max}$ is increased beyond this, the indistinguishability can come back ever so slightly, but even at the first fringe it never exceeds 1%.

This large n limit gives a much higher fraction of indistinguishability than what we calculate for the small numbers of centres. For nanodiamonds of diameter 110 nm, the proportion of spatially indistinguishable emission is 99%. Indeed, a 639 nm nanodiamond (equal diameter to the wavelength) will still have collectivity around 75% in the limit of

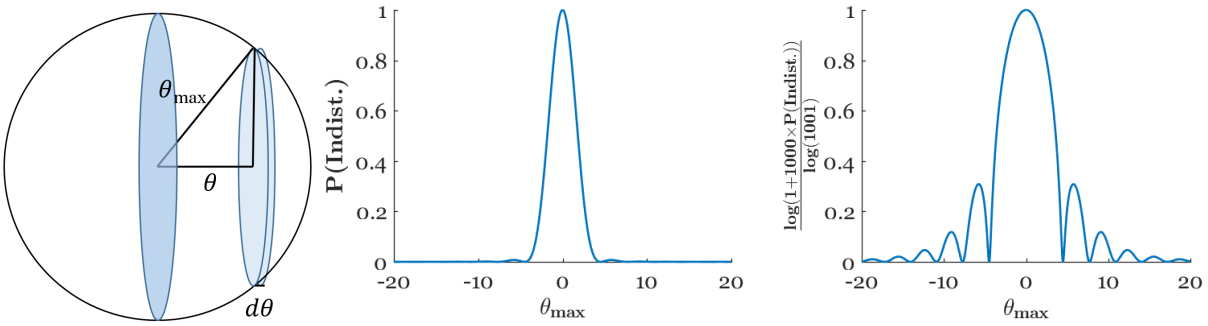

FIGURE 3.8: Left: The probability of any point in a sphere of radius θ_{max} having a distance from the equatorial plane of θ can be calculated as the ratio of the slice of volume with distance θ to the volume of the entire sphere. The slice of volume with distance θ is the cylinder with radius $\sqrt{\theta_{max}^2 - \theta^2}$ and thickness $d\theta$. Centre and Right: Plots of indistinguishability as a function of $\theta_{max} = n_D \vec{k} \cdot \vec{r}_\perp^{(i)}$. The central plot shows the true values of indistinguishability, while the plot on the right has been rescaled to enhance visibility of the peaks.

high densities. This treatment agrees with previous demonstrations that in the case of a pencil-like cloud, superradiance is exhibited most strongly at the extremes of the cloud — corresponding to the $\vec{k}$ vectors for which there is minimal distinguishability [2] [99].

3.4.2 Spectral distinguishability

To determine whether photons are likely to be spectrally distinguishable, we need to determine the likelihood that they have significant overlap in frequency. Photons arising from decay are defined by a Lorenzian which is characterised by an optical linewidth Γ. The central frequency of this decay can vary from centre to centre due to imperfections in the surrounding lattice, including strain, nearby charge traps or foreign atoms. If the spectral separation between two photons is much larger than the linewidth, then they are spectrally distinguishable. If, in contrast, the separation is within the linewidth, photons become gradually indistinguishable (see Figure 3.9).

A natural assumption is to consider NV centres as sufficiently indistinguishable when their transition frequencies do not differ by more optical decay rate, which for our nanodiamonds ranged from $2\pi \times 3.2$ MHz to $2\pi \times 12.7$ MHz, as the optical decay rate is given by the homogeneous linewidth. Sufficiently indistinguishable NV centres form a frequency domain, within which there can be slight variation. In the recent paper, the BJ model determines

the maximal domain size for each of the 100 nanodiamonds examined. While many of the nanodiamonds exhibit maximal domain sizes of one or two, there is a significant fraction of them that require domain sizes of up to 10 to explain the observed decay rates. The fastest nanodiamond identified has a maximum domain size of 50 NV centres.

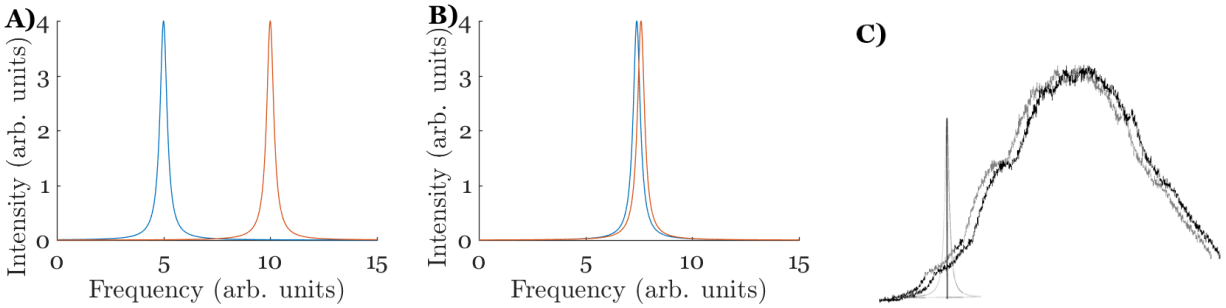

Figure 3.9: A) Distinguishable photons: the spectral separation is five times the linewidth, so the photons are considered distinguishable. B) Indistinguishable photons: the linewidth is five times the separation; qualifying indistinguishability in this case is non-trivial. C) Comparison of widths: The spectrum of a single NV centre gives the ≈ 100 THz envelope in which a photon could be emitted. For multiple NV centres, these spectra can be displaced by ≈ 1 THz. A single photon is given, which has a room temperature linewidth ≈ 1 THz. However, to act collectively, photons must be within the optical decay rate ≈ 10 MHz.

We now consider the scale of the frequencies present. NV centres in bulk diamond have a ZPL at 637 nm with a linewidth of several nm at room temperature, which is on the order of THz [45]. At cryogenic temperatures the linewidth approaches the lifetime-limited value of the optical decay rate, 12.2 MHz [88]. In nanodiamond, we assume that the linewidths of all photons emitted will be similar to the linewidth of the ZPL in bulk. From Fig. 3.1, we see that photons from an NV centre can be emitted anywhere within around a 100-THz window due to phonon broadening. In addition, in different nanodiamonds, the entire spectrum can shift up or down by 1-2 nm, corresponding to THz shifts. Within the same nanodiamond the distribution of transition frequencies is hard to resolve. However, it is likely that the variation in transition frequencies is either less than or equal to the variation in a single diamond. However, as this variance is significantly smaller than the 100-THz range over which a photon can be emitted, it will be neglected. Thus at room temperature, photons with THz linewidth can be emitted with central frequencies anywhere in a 100-THz range. This range is much greater than the MHz range over which NV centres are indistinguishable,

so the small spectral domain sizes are plausible.

Even NV centres in the same frequency domain will not be precisely identical — there will be some small variances between the ZPL frequencies. This was neglected in the BJ model. In our new model, we include it by assigning a unique transition frequency to each NV centre. These frequencies are centred around the ZPL, and follow a Gaussian distribution. The width of the Gaussian distribution should reflect the width over which NV centres are able to act collectively — the optical decay rate.

The energy splitting between the fine structure ground $m_s = 0$ and $m_s = \pm 1$ states is 2.88 GHz [54], while the energy splitting between the fine structure excited $m_s = 0$ and $m_s = \pm 1$ states is 1.42 GHz [100]. This leaves a 1.46 GHz splitting between the $m_s = 0$ transition photons and $m_s = \pm 1$ transition photons. As this splitting is much smaller than the 100-THz variance of ZPL, it implies that $m_s = 0$ and $m_s = \pm 1$ transitions of the same frequency can act collectively. This is distinct from the treatment in the BJ model. To model this collective behaviour between the two spin population requires the full 5-level model.

We have determined that each NV centre can emit photons anywhere within a 100-THz frequency range. This could imply collective domains are not fixed; an NV which emits a photon and is re-excited will be unlikely to emit the second photon into the same spectral domain. Over the course of multiple excitations, many NV centres will each offer a single-photon donation to the collective domain at a particular frequency. However, experiments showed that the individual nanodiamonds exhibited consistent fluorescent behaviour for repeated average measurements, which would contradict the former conclusion. One possibility is that there is some mechanism, supported in only 10% of the diamonds studied, which drives NV centres to emit their photons at an identical frequency. It could be that the collective behaviour causes frequency locking in addition to phase locking. It could otherwise be a phonically driven effect, in which the phonon emitted from one transition induces similar phonons. The energy of a photon + phonon transition must equal the energy of the ZPL transition. Thus, for NV centres of the same ZPL transition, identical phonons must be accompanied by spectrally identical photons. Another possibility is that on average, the statistics play out such that the mean maximum domain size is greater than 50, but in

most diamonds dipole-dipole interactions and dephasing quench the collectivity. This interpretation suggests that "domain size" is actually a measure of the quenching mechanisms. Regardless, from this discussion we see that domain size is unlikely to correspond to a literal number of NV centres which will act cooperatively every time they are excited, but rather it is a figure of merit describing the level of the collectivity observed. In this thesis, we do not attempt to determine the physics underpinning the formation of spectrally identical domains, but we instead focus on how dark decay, orientation effects, dipole-dipole interactions, dephasing, spatial variance and small spectral variation within a domain of collectivity can influence the collective behaviour.

3.5 Number of centres

The dipole-dipole interaction is a pairwise interaction, so for n centres there are $n(n-1)/2$ of these terms to consider. The nanodiamonds studied by our group have a density of $\approx 3\times10^6$ NV centres per μm^3, and a size (110 ± 30) nm, which means around 4000 NV centres per nanodiamond, or 8 million interaction terms. However, it is only a significantly smaller subset of them are interacting cooperatively — estimated to be between $n = 2$ and 50 [6]. As we are interested in the collectively acting NV centres, we only consider these subsets.

In the BJ model interactions with NV centres outside the individual domains are neglected. In our new model, the NV centres in a specific domain are in principle influenced by all other NV centres through dipole-dipole interaction. However, as the dipole-dipole interaction scales inversely with the cube of separation, it is most significant for local NV centres. We thus consider only the collectively acting NV centres, in a smaller nanodiamond such that the density of NV centres is maintained. Thus $n \in \{1, 13\}$ NV centres will be modelled, with a mean separation of 6.93 nm, giving a diameter of $6.93\sqrt[3]{n}$ nm. As the cooperatively acting NV centres are now artificially closer than they would have been, this must be accounted for in the calculation of indistinguishably due to spatial separation by rescaling the distances to reflect their true values.

You make experiments and I make theories. Do you know the difference? A theory is something nobody believes, except the person who made it. An experiment is something everybody believes, except the person who made it.

Albert Einstein

4

Details of the simulation

In this chapter we discuss the two different models used to describe superradiance in NV centres. While I briefly discuss some of the details of the BJ model, the main attention lies on the model developed in this thesis which attempts to include the realistic details of NV centres, as detailed in the previous chapter.

4.1 BJ model

The BJ model is built on Dicke's original construction, assuming maximal symmetry. Each NV centre is modelled as a 2-level spin system, with the ground state $|g_\sigma\rangle$ representing either the $m_s = 0$ the or $m_s = \pm 1$ $^3A_2$ levels, and the excited state $|e_\sigma\rangle$ representing either the $m_s = 0$ or the $m_s = \pm 1$ ^3E levels. Furthermore, the model assumes the $m_s = 0$ and $m_s = \pm 1$ populations to be completely separate. This assumption is questioned in Section 3.4.2.

An ensemble of n NV centres is modelled as a Dicke ladder with $n+1$ levels. In order to account for the known properties of NV centres, dephasing and dark decay are introduced with realistic values. The BJ model neglects the microscopic details and only tracks populations in the collective states $P^{(\sigma)}_{J,M}(t) = \langle J, M, \sigma|\hat{\rho}^{(\sigma)}(t)|J, M, \sigma\rangle$ and in the (non-collective)

single-spin excited states. This works as Dicke superradiance is not dependent on the coherences between Dicke states. Thus, instead of solving the full master equation (Eq. 2.3), the problem is reduced to a set of rate equations. As discussed in section 3.3.2, dephasing occurs

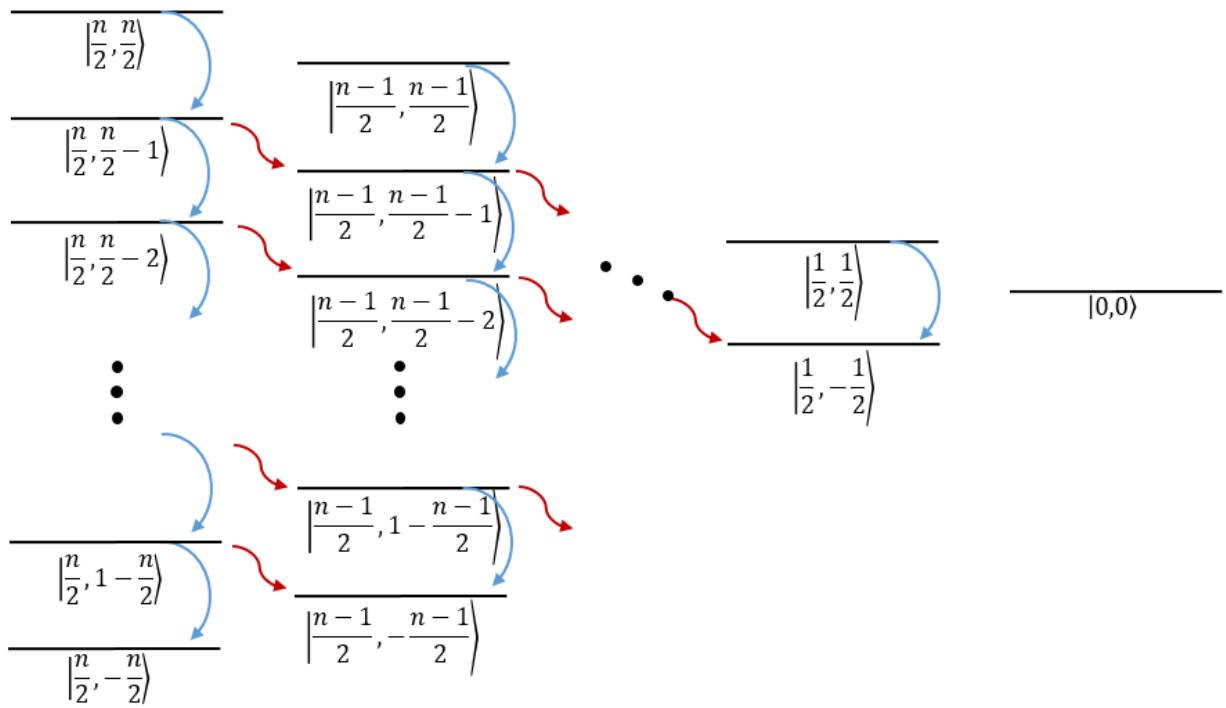

FIGURE 4.1: **Level scheme underlying the BJ model**: Blue lines represent collective decay, red lines represent dephasing into a smaller angular momentum space. There is no dephasing from the $|J, J\rangle$ states as they are eigenstates of the dephasing and projection operators, and are thus unaffected.

because of coupling of the NV centres to the phononic bath and nearby spins. Dephasing at single-spin dephasing rate Γ_d, takes a single centre out of the collective space. Thus with some probability, the collective state $|J, M\rangle$ is projected into a smaller collective state, $|J-1, M-1\rangle$, plus an independent excited centre. The total fluorescence from the system thus consists of emission from both the collective space and the independently decaying centres. In addition, as discussed in Section 3.1, there is dark decay via the singlet states in the

singlet manifold. The additional dark pathways were added to the rate equations as:

$$\begin{aligned}\frac{d}{dt}P^{(\sigma)}_{J,M}(t) = \Gamma \underbrace{(J(J+1)-M(M+1))P^{(\sigma)}_{J,M+1}(t)}_{\text{collective decay in}} - \Gamma \underbrace{(J(J-1)-M(M-1))P^{(\sigma)}_{J,M}(t)}_{\text{collective decay out}} \\ + \Gamma^{(\sigma)}_{dp} \underbrace{2\left(J+\frac{1}{2}\right)\left(1-\left|\frac{M+\frac{1}{2}}{J+\frac{1}{2}}\right|^2\right)P^{(\sigma)}_{J+\frac{1}{2},M+\frac{1}{2}}(t)}_{\text{dephasing in}} - \Gamma^{(\sigma)}_{dp} \underbrace{2J\left(1-\left|\frac{M}{J}\right|^2\right)P^{(\sigma)}_{J,M}(t)}_{\text{dephasing out}} \\ + \Gamma_{\sigma\text{toISC}} \underbrace{(J+M+1)P^{(\sigma)}_{J+\frac{1}{2},M+\frac{1}{2}}(t)}_{\text{dark decay in}} - \Gamma_{\sigma\text{toISC}} \underbrace{(J+M)P^{(\sigma)}_{J,M}(t)}_{\text{dark decay out}}\end{aligned} \tag{4.1}$$

The BJ model explains the experimental observations very well and supports the interpretation of the data in terms of superradiance. It does not capture the complex details of NV centres. Instead it absorbs most of the microscopic details in the heuristic parameter of domain size. As the BJ model is not the main focus of study in this thesis, the interested reader is referred to the superradiance paper for more details [6]. In this thesis we compare the outcomes of the new model with the predictions of the BJ model by numerically solving both alongside each other.

4.2 The new model

The model developed in this thesis sheds new light on superradiance from NV centres, and at the same time provides some comparison to the predictions to the BJ model. In particular, we now include the fact that *(i)* NV centres emit photons into an orientation-dependent superposition of polarizations *(ii)*, NV centres can interact with one another via the permanent and transitional dipole-dipole interactions and *(iii)* NV centres within the same collective domain show a distribution of transition frequencies and spatial locations. Moreover *(iv)*, the effects of phononic coupling are treated here as true dephasing, rather than the phenomenological approach in the BJ model.

The Dicke ladder picture cannot describe symmetry breaking effects, such as dipole-dipole interactions and orientation dependent emission. In our new model, we use the full tensor product space instead. For a 2-level description of n collectively acting NV

centres, instead of a Dicke ladder of states $|n/2, M\rangle$ for $M \in \{n/2, n/2\}$, states are expanded in a basis $|\psi_1\psi_2...\psi_n\rangle = |\psi_1\rangle \otimes |\psi_2\rangle \otimes ... \otimes |\psi_n\rangle$, where $|\psi_i\rangle \in \{|e\rangle, |g\rangle\}$ for the 2-level approximation, $|\psi_i\rangle \in \{|e\rangle, |g\rangle, |ISC\rangle\}$ for the 3-level approximation, and $|\psi_i\rangle \in \{|e_1\rangle, |e_0\rangle, |g_1\rangle, |g_0\rangle, |ISC\rangle\}$ for the 5-level approximation. The density matrix of our system is thus

$$\hat{\rho} = \sum_{\substack{\psi_1\psi_2...\psi_n \\ \psi'_1\psi'_2...\psi'_n}} P^{\psi'_1\psi'_2...\psi'_n}_{\psi_1\psi_2...\psi_n} |\psi_1\psi_2...\psi_n\rangle \langle\psi'_1\psi'_2...\psi'_n| \tag{4.2}$$

where $P^{\psi'_1\psi'_2...\psi'_n}_{\psi_1\psi_2...\psi_n}$ is a matrix element. The total Hamiltonian determines the system and environment's time evolution through the von Neumann equation, $\frac{\partial\hat{\rho}}{\partial t} = -\frac{i}{\hbar}[\hat{H}, \hat{\rho}]$. Over time, the system and the environment becomes entangled. To simplify our problem, we trace over the environmental degrees of freedom to obtain the Born-Markov master equation for the reduced state dynamics of the system of NV centres, with Lindblad terms to account for the interaction of the system with the environment. The derivation of the Born-Markov master equation and its application to similar systems follows the standard procedure [9, 42, 91], and due to the limited space in this thesis it is not presented here. However, construction of the Hamiltonian relevant to our system, its transformation to the rotating frame, the statement of the subsequent master equation in Schrödinger picture and transformation to a frame rotating at the mean transition frequency can be found in Appendix A.

The master equation is numerically solved using MATLAB. In the following we describe the different steps in the simulations. These are: initialization of parameters (Section 4.2.1), configuration of the system (Section 4.2.2), comparative simulations between desired effects (Section 4.2.3), and results, in particular photon emission rates (Section 4.2.4).

4.2.1 Parameters

The program is designed for flexibility. We specify the number of NV centres to be simulated, whether the each NV centre is modelled with 2-, 3- or 5-levels, and in the case of a 2- or 3-level description, which spin system is being modelled ($m_s = 0$ or $m_s = \pm 1$). The physical arrangement (positions and orientations) of NV centres can be chosen, as can the initial state. For most of this thesis we are interested in comparisons with the simulations for the superradiance experiment in Ref. [6], which were done with the BJ model, thus the

parameters can be chosen to replicate any of the four sample nanodiamonds.

4.2.2 Configuration of the system

All the configuration and pre-calculations are done within a MATLAB function file. This involves defining the physical constants and spin matrices, configuring the NV centres within the diamond and giving them an initial state in accordance with the choice made in the previous section, and defining all parts of the master equation.

NV centres corresponding to a single collectively acting domain are distributed in a sphere of diameter $7\sqrt[3]{n}$ nm, which represents the physical size of a diamond of n collectively acting NV centres with density is 3×10^6 NV centres per μm^3, to match nanodiamonds used in the BJ experiment [6]. As the size associated with the n collectively acting NV centres is only used for calculation of the strength of the dipole-dipole interactions, we can simply rescale the dipole-dipole interactions to describe diamonds of other densities. The indistinguishability due to spatial variation is unaffected by this, as it is calculated based on the size of the 110 nm diamond, under the assumption that NV centres are spread across the whole diamond.

Presets in the code allow the spatial distribution to be either random, or in a ring on the xy plane with diameter 2/3 that of the sphere. Each NV centre can be *(i)* randomly assigned one of the eight possible alignments (4 orientations $\times$ 2 directions), *(ii)* oriented along the z axis and randomly aligned in one of the two possible directions, or *(iii)* oriented upwards along the z axis. Random distribution and orientation of NV centres best matches the experimental situation of high-density NV nanodiamonds as used in the BJ paper. The single orientation case is of interest theoretically, as it allows us to simulate observable superradiance with a smaller number of centres. In addition, recent reports indicate the possibility of creating ensembles of NV centres which are parallel [49, 51, 52].

The BJ paper reports autocorrelation measurements that reveal super-Poissonian statistics for the fastest nanodiamonds. This is consistent with the initial state being maximally mixed across the highest J collective space, hereafter referred to as the Dicke mixed state.

In Fig. 4.1, this corresponds to an even mixture of the states on the leftmost Dicke ladder. In our simulations, we study two initial states: the Dicke mixed state and the fully-excited state. The fully-excited state in the 2- and 3-level models corresponds to the state $|\underbrace{ee...e}_{n}\rangle = \underbrace{|e\rangle \otimes |e\rangle \otimes ... \otimes |e\rangle}_{n}$. The Dicke mixed state across $J = n/2$ is

$$\frac{1}{\sqrt{2J+1}} \sum_{M=-J}^{J} |J, M\rangle \langle J, M| \tag{4.3}$$

This can be converted to the product basis via the Clebsh-Gordan coefficients

$$|J, M\rangle = \sqrt{\frac{(M+J)!(J-M)!}{(2J)!}} \sum_{\pi} |\underbrace{g \dots g}_{J-M} \underbrace{e \dots e}_{J+M}\rangle \tag{4.4}$$

The initial state for the 2- and 3-level maximally mixed case is thus

$$\frac{1}{2J+1} \sum_{M=-J}^{J} |J, M\rangle \langle J, M| = \frac{1}{2J+1} \sum_{M=-J}^{J} \frac{(M+J)!(J-M)!}{(2J)!} \sum_{\pi} |\underbrace{g \dots g}_{J-M} \underbrace{e \dots e}_{J+M}\rangle \sum_{\pi} \langle \underbrace{g \dots g}_{J-M} \underbrace{e \dots e}_{J+M}| \tag{4.5}$$

For the 5-level model, NV centres were randomly split into the two spin populations to best reflect the polarization found in the BJ experiment (between 0.5 and 0.56) [6].

The behaviour of the system of NV centres evolving collectively in the presence of environmental dephasing and possible laser excitation is given by the master equation

$$\begin{aligned}
\frac{d\tilde{\rho}}{dt} = &- \underbrace{\frac{i}{\hbar}[\tilde{H}_S + \tilde{H}_{\text{dd}} + \tilde{H}_{\text{per-per}} + \tilde{H}_{SL}, \tilde{\rho}]}_{\text{coherent evolution}} - \underbrace{\frac{\Gamma}{2} \sum_{\sigma} P(\text{Indist.}^{(\sigma)}) \times \mathcal{D}[\hat{S}_{-}^{\sigma}]\tilde{\rho}}_{\text{collective decay}} \\
&- \underbrace{\frac{\Gamma}{2} \sum_{i=1}^{n} \left(1 - \sum_{\sigma} P(\text{Indist.}^{(\sigma)}) P(\sigma|i)\right) \times \mathcal{D}[\hat{s}_{-}^{(i)}]\tilde{\rho}}_{\text{independent decay}} - \underbrace{\sum_{\sigma} \frac{\Gamma_{dp}^{(\sigma)}}{2} \mathcal{D}[\hat{S}_{z}^{\sigma}]\tilde{\rho}}_{\text{global dephasing}} - \underbrace{\sum_{i=1}^{n} \frac{\Gamma_{dp}^{(\sigma)}}{2} \mathcal{D}[\hat{s}_{z}^{(i)}]\tilde{\rho}}_{\text{local dephasing}} \\
&- \underbrace{\frac{\Gamma_{0\text{to}I}}{2} \sum_{i=1}^{n} \mathcal{D}[\hat{s}_{0\text{to}I}^{(i)}]\tilde{\rho} - \frac{\Gamma_{1\text{to}I}}{2} \sum_{i=1}^{n} \mathcal{D}[\hat{s}_{1\text{to}I}^{(i)}]\tilde{\rho}}_{\text{decay from the excited states into the ISC}} - \underbrace{\frac{\Gamma_{I\text{to}0}}{2} \sum_{i=1}^{n} \mathcal{D}[\hat{s}_{I\text{to}0}^{(i)}]\tilde{\rho} - \frac{\Gamma_{I\text{to}1}}{2} \sum_{i=1}^{n} \mathcal{D}[\hat{s}_{I\text{to}1}^{(i)}]\tilde{\rho}}_{\text{decay from the ISC into the ground states}}
\end{aligned} \tag{4.6}$$

where $P(\sigma|i)$ is the proportion of emission into the σ polarisation from the i^{th} atom, defined in Section 3.2. The spin matrices are defined in Appendix A. This equation is written in the frame rotating with respect to ω_0, the angular frequency corresponding to a ZPL of 639 nm.

The first part of the Hamiltonian in Eq. 4.6 describes the bare atomic system

$$\tilde{H}_S = \sum_{i=1}^{n} \hbar(\omega_i - \omega_0)\hat{s}_z^{(i)} \tag{4.7}$$

where ω_i is the angular frequency of the i^{th} NV centre. When choosing not to include spectral inhomogeneity within a collective domain, the ω_i's are all identical, ie $\omega_i = \omega_0 \; \forall \; i \in n$, so this term vanishes. The second part of the Hamiltonian describes the dipole-dipole interaction of the transition dipoles (Eq. 3.4). The third part of the Hamiltonian corresponds to the dipole-dipole interaction of the permanent dipoles (Eg. A.29). The final part of the Hamiltonian describes the interaction of the ensemble with a resonant π polarized continuous laser for the study of superabsorption and is given by

$$\tilde{H}_{SL} = \sum_{i=1}^{n} -\hbar\Omega^{(i)}(\boldsymbol{\varepsilon}^{(i)} \cdot \boldsymbol{\epsilon})\hat{s}_x^{(i)}. \tag{4.8}$$

where $\boldsymbol{\epsilon}$ gives the polarization of the laser and $\Omega^{(i)}$ is the rabi frequency. The remaining terms are the Lindblad terms of the form

$$\mathcal{D}[\hat{S}]\tilde{\rho} = \hat{S}^\dagger\hat{S}\tilde{\rho} + \tilde{\rho}\hat{S}^\dagger\hat{S} - 2\hat{S}\tilde{\rho}\hat{S}^\dagger \tag{4.9}$$

which account for the interaction between the system and the photonic and vibronic environments. All these parts of the master equation can be independently included or excluded to determine their effect on the outcome of the numerical simulation. The laser term is in the simulation to allow for possible later study of superrabsoption.

4.2.3 Evolution

The evolution of the density matrix is found by numerically solving the master equation, including terms as desired. This is done both with the standard MATLAB ODE solver ("ode45"), as well as with a self-coded fourth order Runge-Kutta (rk4) solver. The ode45 solver is faster, but the rk4 solver can handle larger numbers of centres. In addition, using two independent methods provides a check on the correctness and accuracy of the algorithms employed.

ode45 was our first choice for numerically solving the master equation. However, it does have a drawback — like all built-in MATLAB integrators, ode45 is built to solve for scalar-

or vector-valued differential equations, not matrix-valued ones. This is an issue as the master equation describes the differential equation of a matrix (the density matrix). Thus, in order to use ode45, we must first vectorise our system — done by vertically stacking the columns of the density matrix to get a vectorised state $|\hat{p}\rangle$ and using the superspace version of the master equation [101]

$$\frac{d}{dt}|\hat{p}\rangle = [-i(\hat{H}\otimes\hat{I}) + i(\hat{I}\otimes\hat{H}^{\top}) + \Gamma(\hat{J}\otimes\hat{J}^{*}) - \frac{\Gamma}{2}(\hat{J}^{\dagger}\hat{J}\otimes\hat{I}) - \frac{\Gamma}{2}(\hat{I}\otimes\hat{J}^{\top}\hat{J}^{*})]\,|\hat{p}\rangle = \hat{A}\,|\hat{p}\rangle \quad (4.10)$$

where $\hat{J}$ is a general jump operator, and Γ is the associated rate. We have used this approach (albeit with more jump operators) to simulate the master equation. The vectorised state is converted back to matrix form after evolution. At each timestep the vectorised state is stored, and the $\hat{A}$ matrix is determined. The state is a vector of length m^{2n}, where m is the number of levels and n is the number of NV centres. For 10 centres modelled as 2-level systems this number is larger than 1 million; if we instead want use the 5-level model this results in more than 95 trillion elements for every timestep. The $\hat{A}$ matrix then has m^{4n} elements, so for 10 2-level systems this is 10^{12} elements, and for 10 5-level systems it is 9×10^{27} elements. It is only once the system has been solved for the full timespan that the linearised density matrices can each be converted to the two numbers required — the rates of π and σ photon emission. Sparse matrices were used to reduce the memory requirements, but there were still enough non-zero elements to make large calculations prohibitive with the available RAM. The memory requirements of the system can be minimised by passing ode45 a vector of time coordinates to store data for. However, the adaptive timestep means that we can only gain an advantage if we are prepared to sacrifice the quickly varying behaviour.

To simulate as many NV centres as possible, we also solved the master equation with an rk4 integrator, which allowed direct integration of the matrix-valued differential equation and did not require vectorisation. This does not have an adaptive timestep, so it is slower. However, it is much less memory intensive as the matrices involved are all size m^n, and at each timestep we can calculate the rates of π and σ photon emission before solving for the next timestep, so only the density matrix information for the current timestep needs to be stored.

4.2.4 Photon emission

The rate of photon emission can be determined from the number of photons in the optical mode at a given time t, $N(t) = \langle \hat{a}^\dagger \hat{a} \rangle_{\hat{\rho}_E(t)}$. This is determined from the master equation by calculating the excitations in our system, multiplied by the rate of optical decay Γ. If the NV centres are all emitting identical light, this energy is $\langle \tilde{S}_+ \tilde{S}_- \rangle_{\tilde{\rho}} = \mathrm{Tr}(\tilde{\rho} \tilde{S}_+ \tilde{S}_-) = \mathrm{Tr}(\tilde{\rho} \hat{S}_+ \hat{S}_-)$ where $\hat{S}_+$ and $\hat{S}_-$ are the collective raising and lowering operators in the Schrödinger picture. This simplification from rotating frame to Schrödinger frame is possible as our choice of frame rotating with a collective frequency for all centres means that the phases on the raising and lowering operators in the rotating frame $\tilde{S}_+$ and $\tilde{S}_-$ will cancel exactly. This gives the rate of photon emission $dN(t)/dt = \Gamma \mathrm{Tr}(\tilde{\rho} \hat{S}_+ \hat{S}_-)$ However, when multiple NV orientations are included, photons can be emitted into a superposition of polarizations σ. Collective effects only occur within each polarization, so the rate of photon emission is $dN(t)/dt = \Gamma \sum_\sigma \mathrm{Tr}(\tilde{\rho} \hat{S}_+^\sigma \hat{S}_-^\sigma)$. In addition, we have to pay attention to distinguishability of centres introduced by the spatial variance (section 3.3.1). We thus have a fraction of the photons emitted that are indistinguishable, and a fraction which are distinguishable. The total rate of photon emission is therefore given by

$$\Gamma \sum_\sigma P(\text{Indist.}^{(\sigma)}) \mathrm{Tr}(\tilde{\rho} \hat{S}_+^\sigma \hat{S}_-^\sigma) + \Gamma \sum_{i=1}^{n} \left(1 - \sum_\sigma P(\text{Indist.}^{(\sigma)}) P(\sigma|i) \right) \mathrm{Tr}(\tilde{\rho} \hat{s}_+^{(i)} \hat{s}_-^{(i)}). \quad (4.11)$$

The number of photons emitted over time is calculated by numerically integrating Eq. 4.11.

The sciences do not try to explain, they hardly even try to interpret, they mainly make models... The justification of such a mathematical construct is solely and precisely that it is expected to work... Furthermore, it must satisfy certain aesthetic criteria - that is, in relation to how much it describes, it must be rather simple.

John von Neumann

5

Results and discussion

In this chapter we discuss a number of simulation results based on our new model. We go beyond previously explored NV physics and now take into account additional effects, such as dipole-dipole interactions. We determine the level of superradiance for a system starting in the fully excited state by the presence and size of a superradiant 'burst' — a photon emission rate which is initially equal to that for independent emission but then grows to be higher than it. We discuss certain physical aspects of the superradiance from NV centres in detail: the orientation dependence of collective emission (Section 5.1), the impact of the number of levels modelled per NV (Section 5.2), the effect of dipole-dipole interactions, dephasing and spectral and spatial inhomogeneities on a typical domain of NV centres (Section 5.3), and the behaviour when the typical separation between NV centres is decreased (Section 5.4).

5.1 Orientation of NV centres

As discussed in Section 3.2, NV centres of different orientations emit photons into a different superposition of polarizations. Fig. 5.1 provides an example of this; the NV centres

are treated as 2-level systems which are spatially and spectrally indistinguishable, with no dipole-dipole interactions and no dephasing — thus exhibiting superradiance as originally formulated by Dicke. Parallel orientations show typical Dicke superradiance, in which all photons are emitted into the same polarization mode. Random oriented NV centres exhibit decreased superradiance, as photons are emitted into different polarizations, reducing co-operativity. In both cases, the cooperatively acting NV centres show emission rates larger than that of independent emitters, as is characteristic of superradiance. There will however always be some cooperative behaviour, as the possible orientations are not at right angles to each other, so at least one NV centre will have to contribute to both polarization modes.

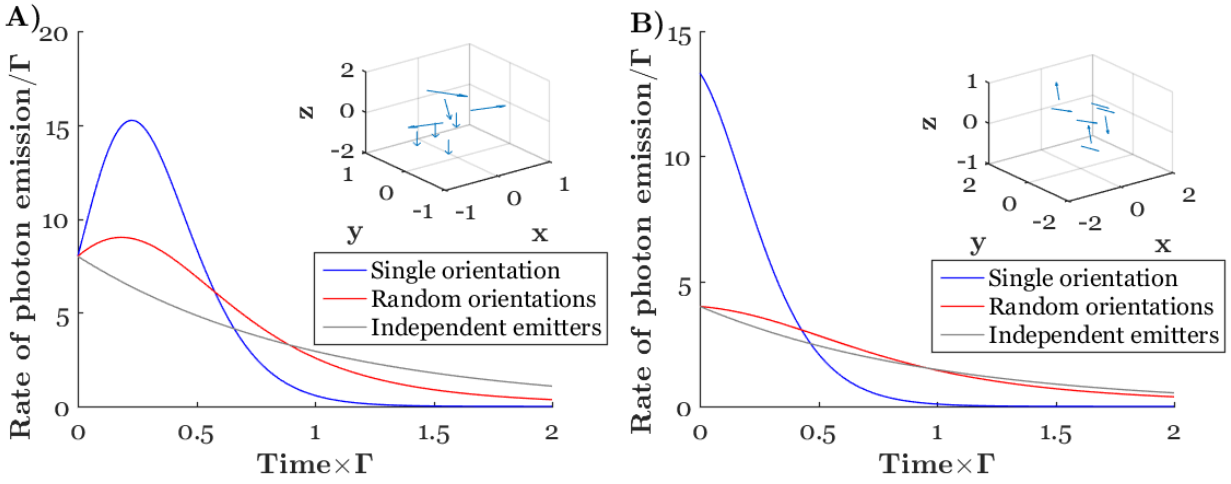

FIGURE 5.1: **Pure Dicke superradiance**: These two plots show Dicke superradiance — collective decay in the absence of dipole-dipole interactions, dephasing, and spatial and distinguishability. 8 NV centres are initialised in the fully-excited state (A) and the Dicke mixed state (B). The insets show the configurations of NV centres for the randomly oriented cases. The x, y and z components have been scaled by the average separation between NV centres. The arrows represent the orientations and locations of the dipoles.

Random orientation does still allow for domains of a single orientation; they have a probability of $1/4^{n-1}$ of occurring. Given the large numbers of domains, there are almost certainly domains which are fully or mostly parallel. This minority of domains is likely responsible for the bulk of the superradiance. With NV centres in diamond engineered to have the same orientation, we would therefore expect stronger superradiant effects. Henceforth, we limit our simulations to NV centres of a single orientation to study the other effects.

5.2 Number of levels

We can model each NV centre with a 2-, 3- or 5-level energy level structure. The 3- and 5-level models include dark decay via the singlet states, reducing the number of photons and consequently the superradiance exhibited.

In Fig. 5.2 A) we compare the 2- and 3- level models. The 2-level model exhibits Dicke superradiance, while in the 3-level model the superradiant burst is clearly reduced due to non-radiative decay via the singlet states. The smaller area under the emission curve indicates the emission of fewer photons in total. The $m_s = 0$ and $m_s = \pm 1$ spin-projection populations show two different bursts as they have separate rates of non-radiative decay. As the rate of optical decay ($2\pi \times 2.5$ MHz) is of similar size to the rate of non-radiative decay from the $m_s = 0$ excited state ($2\pi \times 1.8$ MHz), the superradiant burst for the $m_s = 0$ line is significantly decreased but still remains. In the $m_s = 0$ case, the rate of non-radiative decay ($2\pi \times 9.4$ MHz) is significantly larger, so superradiance is more appreciably quenched. From this, we deduce that the domains most likely to exhibit observable cooperativity are those with all or most NV centres in the $m_s = 0$ state.

In Fig. 5.2 B) we examine four NV centres treated with the 5-level model. We see that for four NV centres (two in each spin state) the collective behaviour is not significantly different to that of independent emitters. This is because the $m_s = \pm 1$ centres rapidly decay to the ground state via predominantly non-radiative means, leaving only two centres decaying cooperatively optically while competing with the non-radiative channels. We conclude that the number of $m_s = 0$ centres in each domain most significantly affects the observed superradiance. Thus, whether or not the $m_s = 0$ and $m_s = \pm 1$ spin projection centres act collectively with each other, which was debated in Section 3.4.2, becomes a non-critical issue.

While the 3- and 5-level models reflect the physics of the NV centre more accurately, they make the simulations more challenging in terms of computational demand. For this thesis, simulation were performed on a desktop computer, so we choose to concentrate on computationally easier problems. Thus to simulate a larger number of spins, we focus on the 2-level model. This allows us to simulate more NV centres and to eliminate the non-radiative

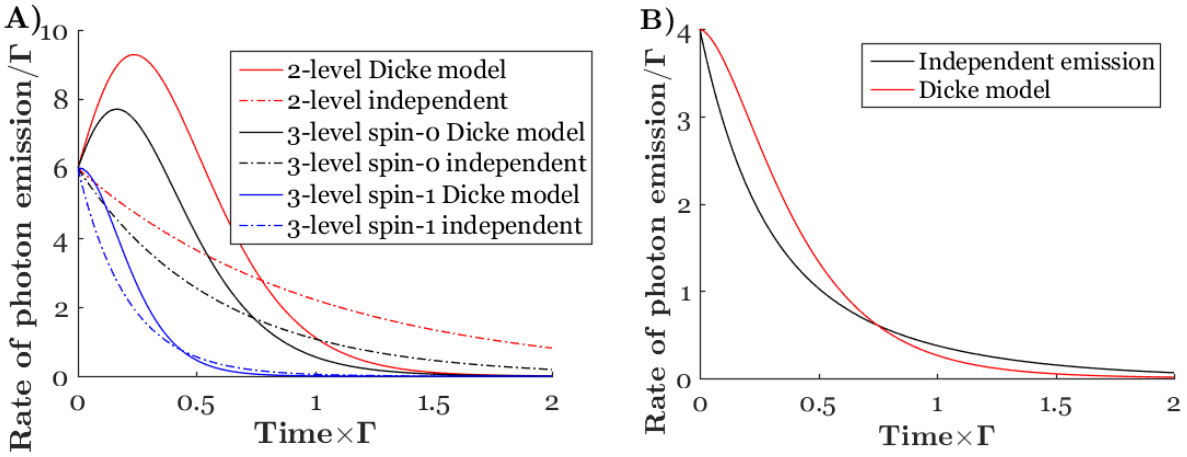

FIGURE 5.2: **Changing the number of levels modelled:** A) the rate of photon emission from 6 parallel fully excited NV centres is shown, modelled as 2- and 3-level systems. B) the rate of photon emission from 4 parallel fully excited NV centres modelled as a 5-level system is depicted. Two of these NV centres start in the $m_s = 0$ state and two start in the $m_s = \pm 1$ state. The independent emission line is modelled by considering a single NV centre in an equal superposition of the $m_s = 0$ and $m_s = \pm 1$ excited states. The ratio of $m_s = 0$ to $m_s = \pm 1$ states was chosen to best reflect the ratio found in the experiment.

paths which decrease superradiance. We stress that in our subsequent simulations, as we neglect the non-radiative decay, our simulations are not directly comparable with experimental results. We use the 2-level model to gain insight into the way different details of the NV centres effect the collective behaviour, relative to one another. To compare to experiment, the 5-level models should instead be used. However, due to the rapid non-radiative decay from the $m_s = \pm 1$ excited state which quenches majority of the superradiance, the 3-level model of just the $m_s = 0$ state provides a reasonable picture of the superradiance decay.

5.3 A typical domain of NV centre

In Fig. 5.3 we examine the effects of dipole-dipole interactions, dephasing and spatial and spectral variance. Limiting our discussion to parallel 2-level NV centres, we examine 8 NV centres starting in the fully excited state. We see that dipole-dipole interactions, dephasing and spatial and spectral variance can significantly reduce the overall superradiance. The spatial variance explicitly reduces the overall collectivity. The spectral variance introduces non-uniform local dephasing which, like the normal local dephasing, decoheres the system

towards independent behaviour. Both dipole-dipole interactions are shown to have strong effects. In fact, for NV centres separated by a mean of 7 nm, as is typical of our diamonds [6], the permanent dipole-dipole interaction completely quenches any superradiance. The BJ model is not well fitted by the dephasing model, let alone the all effects model. This suggests that the BJ model is an insufficient description when dipole-dipole interactions are included at this density.

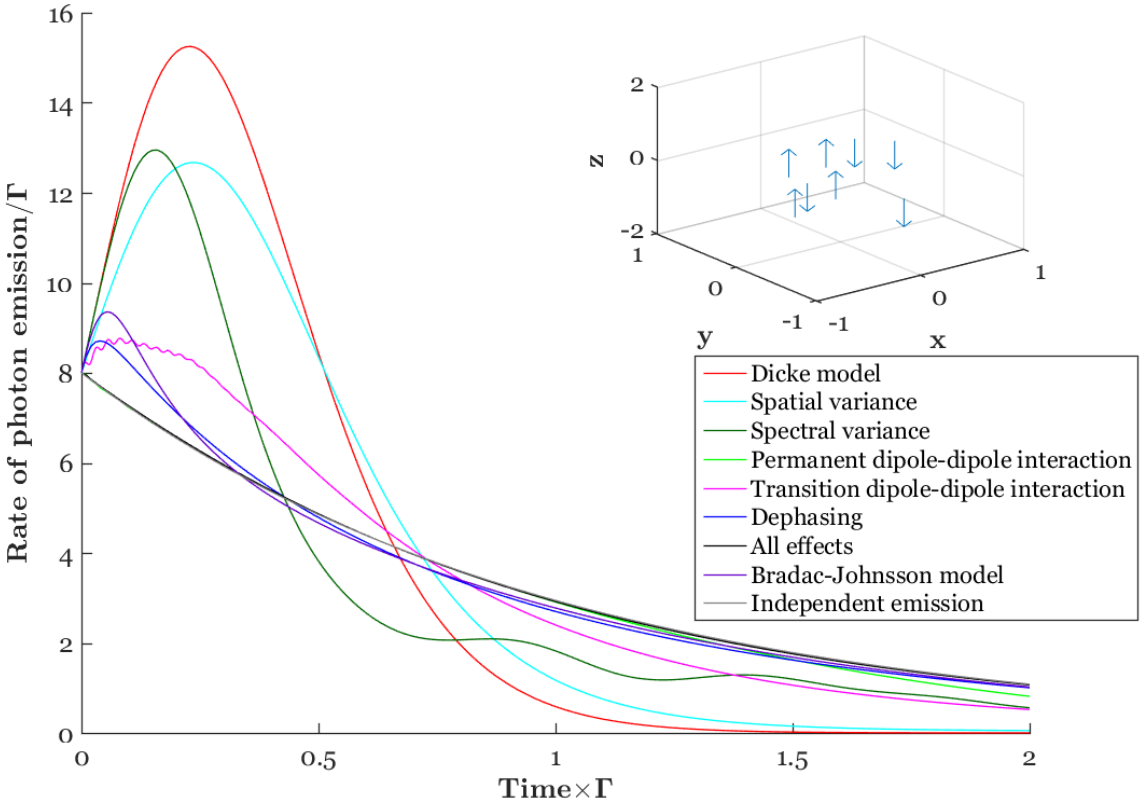

FIGURE 5.3: **Quenching superradiance**: 8 NV centres starting in the fully-excited state are simulated. The effect of incorporating each realistic aspect of the NV centre individually and the result of combining all these effects are shown. The permanent dipole-dipole interaction line, the all effects line and the independent emission line lie on top of one another, indicating that the permanent dipole-dipole interaction has quenched all collective behaviour. The BJ model (with the non-radiative decay rate set to 0) is shown for comparison.

This result shows us that at this density, a domain of NV centres is unlikely to exhibit superradiance. This agrees with experimental findings that $\sim 10\%$ of the nanodiamonds studied exhibited any evidence of collective behaviour, and even then, they generally had

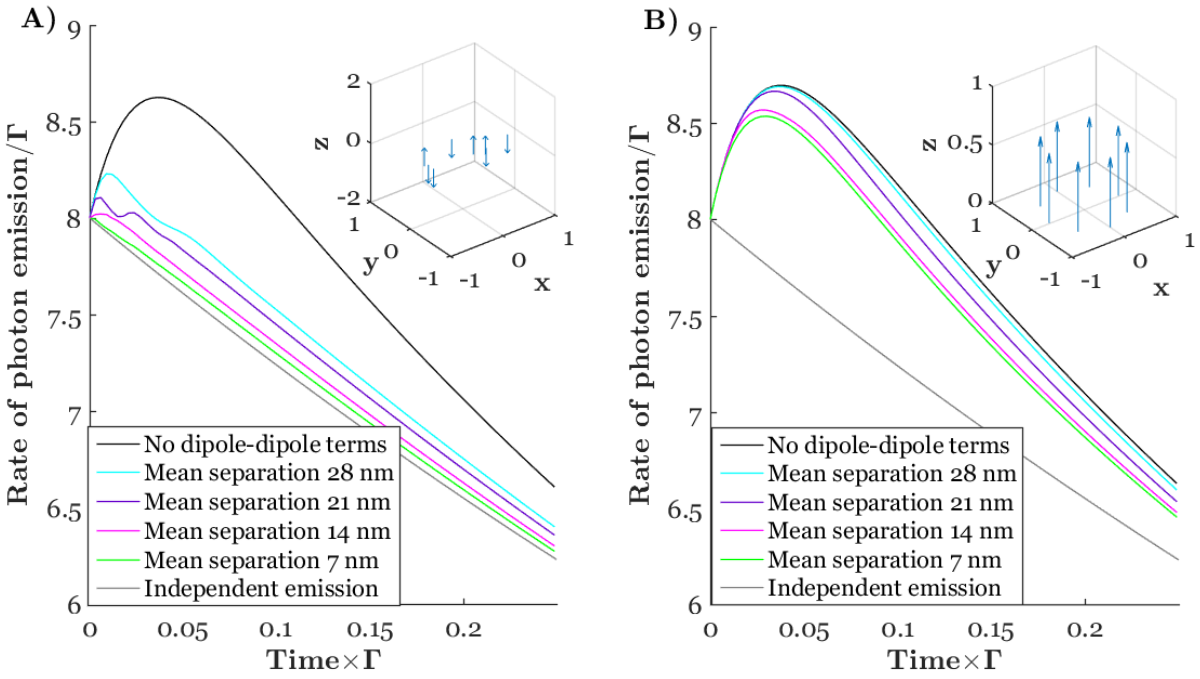

FIGURE 5.4: **Increasing the separation**: Rate of photon emission with all effects for varying separations between 8 parallel NV centres which are A) randomly distributed and B) in a ring.

only a small number of NV centres per domain.

5.4 Varying the NV typical separation

We see in Fig. 5.3 that superradiance is most significantly quenched by dipole-dipole interactions, which scale inversely with the cube of separation. The density of NV centres we chose was informed by the typical density in the diamond studied. Within and between the diamonds there is natural variation in the exact number and distribution of NV centres. In Fig. 5.4 we see the effect of the spacing of NV centres. In these plots, we have included all the effects in each run, however we have varied the mean separation of dipoles by uniform expansion of the physical system. In the plot on the left, we show a random configuration of NV centres. As the separation grows by factors of 2, 3 and 4, the dipole-dipole terms are reduced by factors 2^3, 3^3 and 4^3, respectively. This reduction allows greater superradiance, as is indicated by the gradual return of the superradiance 'burst'.

In the figure on the right we consider a symmetric arrangement where parallel NV centres

are equally spaced in a ring perpendicular to their orientation. This configuration would be extremely unlikely to occur naturally. However, this configuration is interesting to consider for the study of isolated effects, and as it is one which could be engineered. There is an extensive body of work surrounding the creation of diamond with NV centres in specific locations [47, 48, 64, 102–107]. To date, NV centres can be can be placed at specific sites, up to an error on the order of 10 nm. For our purposes, this error is too high. Nonetheless, if NV centres are created in a ring, they could potentially be aligned to lie on the same orientation by strain engineering [52] or atomistic mechanisms [108]. In Fig. 5.3 we short-cut all the engineering difficulties by simulating the behaviour of 8 parallel NV centres in a ring. Here, a mean separation of r between centres results in a diamond of size $2r$. The ring radius $r/3$, gives the separation between centres to be $\pi r/6$. By observing the photons from directly above or below this ring, the geometry ensures that the path lengths between each NV and the detector will be identical, so the spatial indistinguishability is guaranteed. The superradiance burst in the plot on the right is higher than those with dipole-dipole interactions in previous figures, indicating that the symmetry of the system preserves far more superradiance than the random arrangement case. Again, by increasing the spacing, superradiance is enhanced.

In Fig. 5.5, we examine how our new model compares to the Dicke model, to the BJ model, and to independent emission. The simulation of 8 NV centres is initialized in the Dicke mixed state to see how these models would provide a different interpretation of the experimental behaviour. To examine the situation where dipole-dipole interactions are not overpowering, we choose a mean separation of 21 nm. Such a large mean separation is unlikely to occur for the diamonds with the densities of our experiments, but exhibits more superradiance if it does occur. Comparing Dicke superradiance with the independent emission, we see that Dicke superradiance exhibits a steeper slope. The more centres in the collectively acting domain, the bigger this disparity. However, in Fig. 5.5 we also see the realistic details of an NV centre — dipole-dipole interactions, dephasing, spatial and spectral inhomogeneities — cause an even greater slope. This is because the system is very quickly decohering out of the collectively acting states to return to independent behaviour. The most

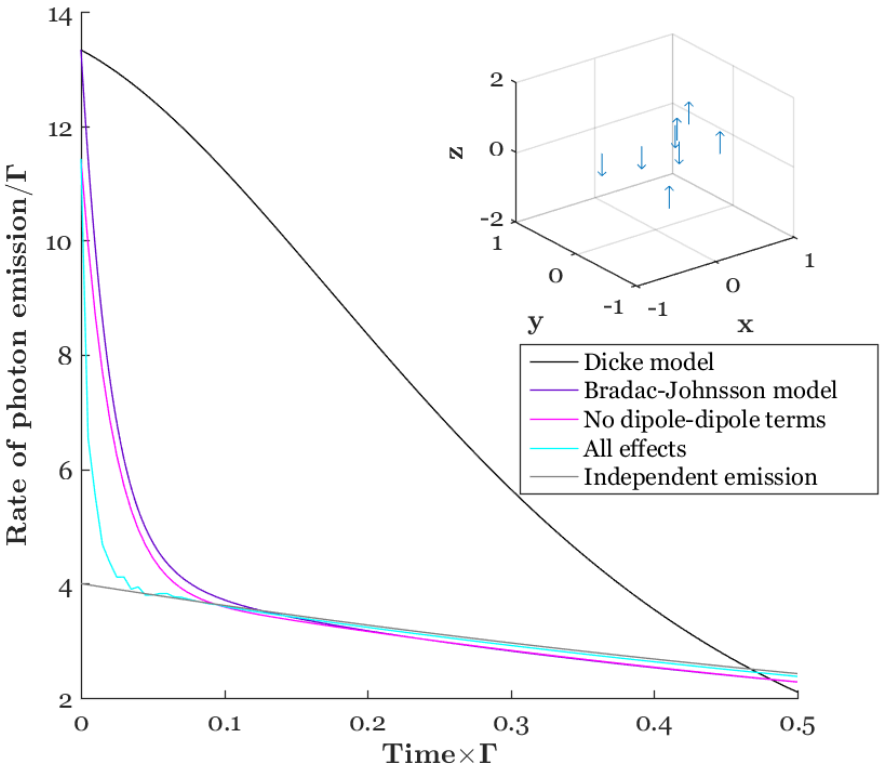

FIGURE 5.5: **Recovering superradiance**: Here we consider a fortuitous configuration of 8 NV centres, in which the typical separation between NV centres is 21 nm (as opposed to 7 nm), which allows for some superradiance to persist. The simulation is started in the Dicke mixed state, which corresponds to the initial state in the experiments. We have limited the NV centres to one orientation, but their spatial distribution and alignment with the z axis (parallel or anti-parallel) is random.

dramatic effect is the dipole-dipole interaction, which is the most sensitive to the configuration of NV centres in the diamond. Consider again Fig. 2.2, containing the experimental results for the nanodiamonds studied. If there is no collective behaviour, the emission must follow the single NV line. However, by varying the dipole-dipole interaction, a domain of any size can be made to have an arbitrarily steep gradient. Thus while independent emission cannot cause a steep slope, the steepness of the slope is not sufficient to determine domain sizes. This is why, in the BJ paper, the domain sizes were further confirmed with $g^2(0)$ correlation measurements. We have not yet completed $g^2(0)$ calculations as part of this work, but intend to do so.

We have determined that superradiance is more likely to occur when NV centres are well

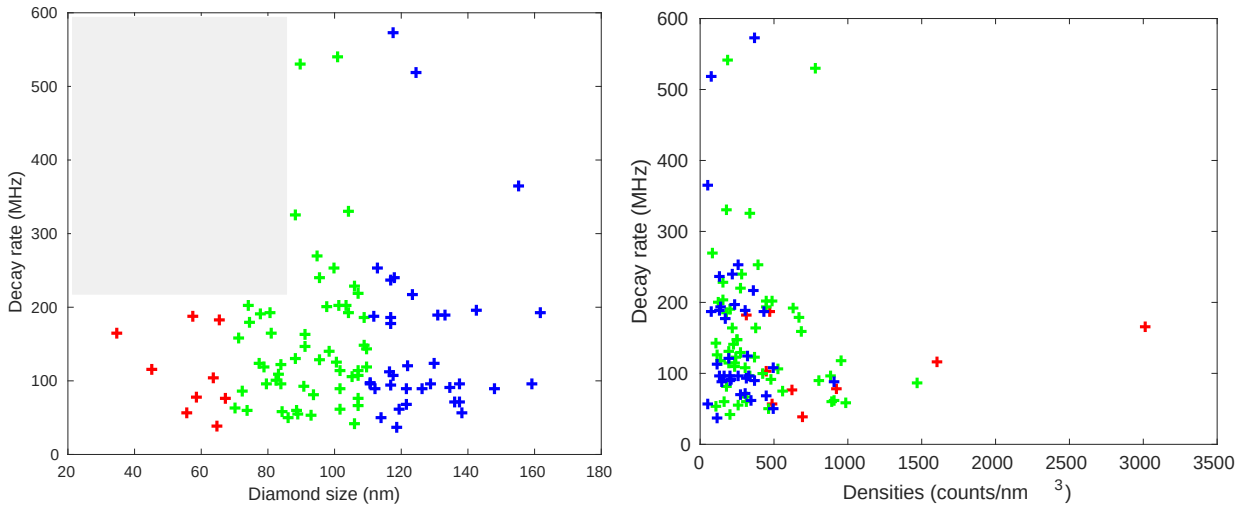

Figure 5.6: The decay rate as a function of diamond size (left) and density (right) for each of the 100 nanodiamonds in the experiments our group undertook. The densities were measured via continuous fluorescence measurements and are thus in arbitrary units. The colour coding corresponds to the size of the diamonds, with red $<$ 70 nm $<$ green $<$ 110 nm $<$ blue. Figures from Ref. [6].

separated from their neighbours. In practice, increasing the spacing comes at cost of either increasing the size of the diamond, and hence introducing more distinguishability due to spatial separation, or of decreasing the number of NV centres in the diamond, and hence the number and size of collective domains. In Fig. 5.6 from Ref. [6], we determine that nanodiamonds below 80 nm are unlikely to exhibit superradiance, but above this threshold there is no strong relation between size and density. This is shown by plotting decay rate as a function of diamond size. As is discussed above, decay rate is not perfectly correlated with the amount of superradiance, but a faster than exponential decay rate is always present when there is any collective behaviour. This is consistent with our modelling which shows that as the size of the nanodiamond increases, the increased likelihood of collectively acting domains is counteracted by the increased distinguishability due to spatial separation. In the paper [6], we also determine that nanodiamonds with high densities (measured via the total photons detected) cannot have large decay rates, meaning they are not exhibiting superradiance. This is consistent with our findings above that high densities prevent superradiance as the dipole-dipole interactions become too large.

5.5 Summary of results

Through simulation, we are able to explore the rich tapestry of effects in NV centres. We find that randomly-oriented NV centres exhibit significantly less superradiance than parallel centres.

We considered 2-, 3- and 5-level models of the NV centre. While the 5-level model is most realistic, the rapid rate of dark decay from the $m_s = \pm 1$ state means that it is domains of predominantly $m_s = 0$ systems which contribute to superradiance. This means that where we want to study the domains contributing to the observed superradiance, the 3-level model is sufficient. In practice however, we tended to simulate the 2-level model, as this still provides information about relative influence of microscopic physics on the emission rates.

Each of the effects we studied, spatial and spectral variance, dephasing and dipole-dipole interactions, reduced superradiance. The most significant is the permanent dipole-dipole interaction which, for the typical spacing of NV centres in our diamonds, completely quenches the superradiance. However, in engineered arrangements where the NV centres have a lower density than for those used in our experiments, we see that the subsequent decrease in the dipole-dipole terms permits superradiance to survive. This is consistent with the experimental findings that nanodiamonds of high densities will not exhibit superradiance.

[Kepler] had to realize clearly that logical-mathematical theorising, no matter how lucid, could not guarantee truth by itself; that the most beautiful logical theory means nothing in natural science without comparison with the exactest experience. Without this philosophic attitude, his work would not have been possible.

Albert Einstein

6

Outlook

In this thesis we have developed a mathematical model to simulate superradiance from NV centres. With this model, we determine that superradiance can exist in NV-rich nanodiamonds, but in the presence of orientation effects, non-optical decay, dipole-dipole interactions, dephasing and spatial and spectral inhomogeneity, it is elusive. Far from being guaranteed, superradiance occurs under specific circumstances, in certain spatial arrangements and for particular densities of sufficiently indistinguishable NV centres. This is consistent with the experimental findings in the BJ paper that superradiance is exhibited in $\sim 10\%$ of nanodiamonds studied. Of the effects considered, the optical and permanent dipole-dipole interactions are responsible for the most significant quenching of superradiance at the NV centre densities used in the experiments. We find that for these densities, the phenomenological dephasing description in the BJ model is insufficient to properly describe these interactions.

In addition to studying superradiance observed in the BJ experiment, this work can be used to inform the engineering of enhanced superradiance. We predict that nanodiamonds with parallel NV centres in slightly lower densities than those used in Ref. [6] will exhibit stronger superradiance.

Further work remains to transition this simulation from toy model into a more accurate representation of the fundamental physics of NV centres. For instance, the spatial variance could be treated explicitly, and the spatial distribution of emitted light explored. Understanding the spectral distinguishability of photons arising from the phonon-broadened optical spectrum of NV centres remains a topic of future study.

Another area of future work is to adapt our model to predict the occurrence and strength of superradiance in other diamond defects, such as SiV and GeV centres. These are particularly interesting as they do not have the permanent dipole-dipole interaction which was the single most destructive effect studied. However, superradiance in SiV and GeV centres may be hindered by other effects, such low quantum efficiencies. Whether these competing effects will ultimately yield higher levels of superradiance remains an open question. We can similarly adapt our model to describe low-temperature physics. Although the effect of dephasing from phonon-coupling will be reduced, the question of whether this will result in enhanced superradiance is again not obvious, since spin-orbit coupling makes some optical transitions more distinguishable. The results predicted through this future work can be experimentally tested — I personally aim to conduct a theoretical and experimental study into superradiance in SiV centres.

We would also like to study superabsorption [42], and examine whether NV (or other) centres are a viable system for the demonstration and applications of this phenomenon.

In addition, further research includes developing more sophisticated numerical techniques to increase the number of NV centres that can be modelled, such as writing a more sophisticated integrator, running the simulations on a supercomputer, or using quantum trajectories.

The work done in this thesis represents a significant advance from the BJ model, allowing a richer description of superradiance from NV centres. Through improvements to the model and adaptation to different systems, we hope to shed further light into cooperative behaviours in NV centres and similar diamond defects.

It is the theory which decides what we can observe.

Albert Einstein

A

Formulation of the master equation

The Hamiltonians are defined in the Schrödinger picture and transformed to the Dirac picture for the rotating wave approximation and the derivation of the Born-Markov Master equations. The Born-Markov Master equation is not derived as it is a well-known result, and as this thesis is subject to a tight page limit; instead the general result is applied to our system. The resultant master equation is converted to a new frame for simulation.

A.1 Definitions of NV centre operators

The excited and ground states of a single NV centre modelled as a 2-level atom are represented as $|e\rangle = (1\ 0)^\top$ and $|g\rangle = (0\ 1)^\top$ respectively. The spin $n/2$ matrices are used to represent n centres acting collectively. These matrices are conventionally defined as having a factor of $\hbar$, but in this thesis we use a $\hbar$-less form. For spin 1/2, these matrices are $\hat{s}_x = \frac{1}{2}(|g\rangle\langle e| + |e\rangle\langle g|)$, $\hat{s}_y = \frac{i}{2}(|g\rangle\langle e| - |e\rangle\langle g|)$ and $\hat{s}_z = \frac{1}{2}(|e\rangle\langle e| - |g\rangle\langle g|)$, The ladder operators, $\hat{s}_+ = |e\rangle\langle g|$ and $\hat{s}_- = |g\rangle\langle e|$, represent the creation and destruction of excitations in the system. We also introduce the matrix $\hat{s}_e = |e\rangle\langle e|$.

For the 3-level system, an additional level is introduced representing the intermediate singlet levels, denoted I, giving $|e\rangle = (1\ 0\ 0)^\top$, $|g\rangle = (0\ 1\ 0)^\top$ and $|I\rangle = (0\ 0\ 1)^\top$. The 3-level operators have the same bra/ket expressions as the 2-level operators, with the exception of the new operators which we must introduce to describe a transformation from the excited state to the I level $\hat{s}_{\text{to}I} = |I\rangle\langle e|$ and from I to the ground states $\hat{s}_{\text{from}I} = |e\rangle\langle I|$.

For the 5-level system, each operator can act on the $m = 0$ subspace or on the $m = \pm 1$ subspace. For a single centre, the possible states are $|e_1\rangle = (1\ 0\ 0\ 0\ 0)^\top$, $|e_0\rangle = (0\ 1\ 0\ 0\ 0)^\top$, $|g_1\rangle = (0\ 0\ 1\ 0\ 0)^\top$, $|g_0\rangle = (0\ 0\ 0\ 1\ 0)^\top$ and $|I\rangle = (0\ 0\ 0\ 0\ 1)^\top$. The new operators which act on spin-1 centres are $\hat{s}_{1,x} = \frac{1}{2}(|g_1\rangle\langle e_1| + |e_1\rangle\langle g_1|)$, $\hat{s}_{1,y} = \frac{i}{2}(|g_1\rangle\langle e_1| - |e_1\rangle\langle g_1|)$, $\hat{s}_{1,z} = \frac{1}{2}(|e_1\rangle\langle e_1| - |g_1\rangle\langle g_1|)$, $\hat{s}_{1,+} = |e_1\rangle\langle g_1|$, $\hat{s}_{1,-} = |g_1\rangle\langle e_1|$and $\hat{s}_{1,e} = |e_1\rangle\langle e_1|$. and the new operators which act on spin-0 centres are $\hat{s}_{0,x} = \frac{1}{2}(|g_0\rangle\langle e_0| + |e_0\rangle\langle g_0|)$, $\hat{s}_{0,y} = \frac{i}{2}(|g_0\rangle\langle e_0| - |e_0\rangle\langle g_0|)$, $\hat{s}_{0,z} = \frac{1}{2}(|e_0\rangle\langle e_0| - |g_0\rangle\langle g_0|)$, $\hat{s}_{0,+} = |e_0\rangle\langle g_0|$, $\hat{s}_{0,-} = |g_0\rangle\langle e_0|$ and $\hat{s}_{0,e} = |e_0\rangle\langle e_0|$ Frequently operators will act on both subspaces; these are denoted $\hat{s} = \hat{s}_1 + \hat{s}_0$. As for the 3-level case, we also require operators which transform from the excited states to the I level $\hat{s}_{1\text{to}I} = |I\rangle\langle e_1|$ and $\hat{s}_{0\text{to}I} = |I\rangle\langle e_0|$ and from the I level to the ground states $\hat{s}_{I\text{to}1} = |e_1\rangle\langle I|$ and $\hat{s}_{I\text{to}0} = |e_0\rangle\langle I|$.

To describe n NV centres, the Hilbert space of each system is tensored together giving $\mathcal{H} = \mathcal{H}_1 \otimes \mathcal{H}_2 \otimes ... \otimes \mathcal{H}_n$. From the single centre operators, ***local*** and ***global*** operators can be constructed. Local operators act on an individual centre i as $\hat{s}^{(i)} = \mathbb{1}_{m^{i-1}} \otimes s \otimes \mathbb{1}_{m^{n-i}}$ while global operators act on all centres together as $\hat{S} = \sum_{i=1}^{n} \hat{s}^{(i)}$ where n is the number of centres being modelled, and m is the number of levels each centre is modelled as having.

A.2 Hamiltonian in the Schrödinger picture

The Hamiltonian can always be decomposed into a system part, an environment part and an interaction between these two parts. In our case, the system describes the ensemble of n NV centres, and the environment describes surrounding electric fields. This includes the vacuum field, the laser field (for superabsorption only) and the electric field created by the permanent electric dipoles of NV centres in their excited states. In addition, there is a static electric field arising from stray charges in the nanodiamond, which gives rise to energy shifts in the

NV centres. However, in our modelling spectral inhomogeneity is accounted for separately, so we will neglect this term here.

A.2.1 The system part of the Hamiltonian

For the 2-level case, each i^{th} NV centre has the bare Hamiltonian $\hat{H}_S^{(i)} = E_e^{(i)} |e\rangle_i \langle e| + E_g^{(i)} |g\rangle_i \langle g|$ where E_e is the energy of the excited state and E_g is the energy of the ground state. By subtracting $\frac{E_e^{(i)}+E_g^{(i)}}{2} \times \mathbb{1}$ and defining $\omega_i = \frac{E_e^{(i)}-E_g^{(i)}}{\hbar}$, the equivalent form $\hat{H}_S^{(i)} = \hbar\omega_i \hat{s}_z^{(i)}$ is obtained. Thus the bare Hamiltonian describing the n spin-1/2 systems can be expressed

$$\hat{H}_S = \sum_{i=1}^{n} \hbar\omega_i \hat{s}_z^{(i)}. \tag{A.1}$$

For the 3 and 5-level systems, the energy of the additional levels must be accounted for. The bare Hamiltonian describing the energy levels for the 3-level case is

$$\hat{H}_S = \sum_{i=1}^{n} E_e^{(i)} |e\rangle_i \langle e| + E_g^{(i)} |g\rangle_i \langle g| + E_I^{(i)} |I\rangle_i \langle I| \tag{A.2}$$

and the bare Hamiltonian describing the energy levels for the 5-level case is

$$\hat{H}_S = \sum_{i=1}^{n} E_{e_1}^{(i)} |e_1\rangle_i \langle e_1| + E_{g_1}^{(i)} |g_1\rangle_i \langle g_1| + E_{e_0}^{(i)} |e_0\rangle_i \langle e_0| + E_{g_0}^{(i)} |g_0\rangle_i \langle g_0| + E_I^{(i)} |I\rangle_i \langle I| . \tag{A.3}$$

A.2.2 The environment part of the Hamiltonian

The environment we wish to model includes the vacuum field, the laser field (for superabsorption only) and the electric field created by the permanent electric dipoles of NV centres in their excited states.

The part of the Hamiltonian corresponding to the vacuum field is

$$\hat{H}_E = \sum_j \hbar\omega_j \hat{a}_j^\dagger \hat{a}_j. \tag{A.4}$$

where $j = \{\mathbf{k}, \sigma\}$ is the tuple summarising the k vector $\mathbf{k}$ and a polarization σ of the photon.

If there is a laser, it is treated as a coherent state. Coherent states are defined mathematically as $\hat{a} |\alpha\rangle = \alpha |\alpha\rangle$ where α is a complex number with $|\alpha|^2$ representing the mean number of photons in the state. To describe a laser, the coherent state has a time dependence

$\exp(-i\omega_L t)$. Thus at the frequency of the laser, ω_L, $\hat{a}_{\mathbf{k}_L,\sigma} \to \hat{a}_{\mathbf{k}_L,\sigma} + \alpha_\sigma \exp(-i\omega_L t)$, where α is a coherent laser light state with k vector $\mathbf{k}_L$ and polarization $\sigma \in \{\pm 1, 0\}$. Thus

$$\hat{H}_L = \sum_\sigma \hbar\omega_L(\alpha^*_\sigma \hat{a}_{\mathbf{k}_L,\sigma} \exp(i\omega_L t) + \alpha_\sigma \hat{a}^\dagger_{\mathbf{k}_L,\sigma} \exp(-i\omega_L t)) + \sum_\sigma \hbar\omega_L \alpha^*_\sigma \alpha_\sigma \tag{A.5}$$

The final term is an energy shift, so it can neglected defining the zero energy state of the environment to be $-\sum_\sigma \hbar\omega_{\lambda_L}\alpha^*_\sigma\alpha_\sigma$.

As we are interested in the optical phenomena, we will only consider the electric field in the context of its interaction with the collection of NV centres.

A.2.3 The interaction part of the Hamiltonian

The interaction between the NV centres and the field is described using the dipole approximation. For the i^{th} particle at position $\mathbf{r}_i$ and time t, interacting with the j^{th} mode of the EM field, this interaction is described by

$$\hat{H}^{(i,j)}_{\text{int}} = -\hat{\mathbf{d}}^{(i)} \cdot \mathbf{E}_j(\mathbf{r}_i, t) \tag{A.6}$$

where $\hat{\mathbf{d}}^{(i)}$ is the dipole moment operator of the NV centre, and $\mathbf{E}_j(\mathbf{r}_i, t)$ describes the EM field.

Dipole term

The dipole operator $\hat{\mathbf{d}} = q\hat{\mathbf{r}}$ is analogous to its classical counterpart, where the displacement operator $\hat{\mathbf{r}}$ takes the operator information.

For a *typical* quantum optics system, the only dipole moment of interest is the transition dipole moment, $\hat{\mathbf{d}}^{(i)}_{eg}$, describes the electric transition between the ground an excited states. The argument goes that can be expanded in the 2-level basis

$$\begin{aligned}
\hat{\mathbf{d}}_i &= \mathbb{1}\hat{\mathbf{d}}_i\mathbb{1} \\
&= (|g\rangle_i \langle g| + |e\rangle_i \langle e|)\, \hat{\mathbf{d}}_i\, (|g\rangle_i \langle g| + |e\rangle_i \langle e|) \\
&= |g\rangle_i \langle g|\, \hat{\mathbf{d}}_i\, |g\rangle_i \langle g| + |g\rangle_i \langle g|\, \hat{\mathbf{d}}_i\, |e\rangle_i \langle e| + |e\rangle_i \langle e|\, \hat{\mathbf{d}}_i\, |g\rangle_i \langle g| + |e\rangle_i \langle e|\, \hat{\mathbf{d}}_i\, |e\rangle_i \langle e|
\end{aligned} \tag{A.7}$$

$|g\rangle$ and $|e\rangle$ are eigenstates of the parity operator $\hat{P}$, meaning that $\hat{P}|g\rangle = |g\rangle$ and $\hat{P}|e\rangle = |e\rangle$

However, the parity operator clearly inverts the displacement operator as $\hat{P}\hat{\mathbf{r}}\hat{P} = -\hat{\mathbf{r}}$. Combining these relations, it is evident that the diagonal terms of the dipole moment operator must vanish.

$$\langle g|\,\hat{\mathbf{d}}\,|g\rangle = \langle g|\,q\hat{\mathbf{r}}\,|g\rangle = \langle g|\,\hat{P}q\hat{\mathbf{r}}\hat{P}\,|g\rangle = -\langle g|\,q\hat{\mathbf{r}}\,|g\rangle = -\langle g|\,\hat{\mathbf{d}}\,|g\rangle = 0 \tag{A.8}$$

Also, ${}_i\langle g|\,\hat{\mathbf{d}}_i\,|e\rangle_i$ is the transition dipole moment which describes the electric dipole moment associated with the transition from the excited to the ground state. Similarly, ${}_i\langle e|\,\hat{\mathbf{d}}_i\,|g\rangle_i$ is the transition dipole moment which describes the electric dipole moment associated with the transition from the ground to the excited state. By conservation of energy, these must be the same, and they will both be abbreviated to $\mathbf{d}_{eg}^{(i)}$. This gives the result

$$\hat{\mathbf{d}}_i = \mathbf{d}_{eg}^{(i)}(|g\rangle_i\langle e| + |e\rangle_i\langle g|) = 2\mathbf{d}_{eg}^{(i)}\hat{s}_x^{(i)}. \tag{A.9}$$

The transition dipole operator has magnitude $d_{eg} = 2.980^{-30}$ C m, as calculated in Section 3.3.1.

However, NV centres are an atypical quantum optics system, as the ground and excited states are *not* eigenstates of parity. This is because the NV centre does not have inversion symmetry. Thus the NV centre doesn't have vanishing diagonal dipole moment terms. In fact, for the excited state, the NV centre has a very strong permanent dipole moment of magnitude $d_{\text{per}} = 3.976 \times 10^{-30}$ C m, which is aligned with dangling bond from the nitrogen atom to the direction of the vacancy [87, 88]. We will treat this as a separate dipole operator, $\hat{\mathbf{d}}_{\text{per}}^{(i)} = \mathbf{d}_{\text{per}}^{(i)}|e\rangle\langle e|^{(i)} = \mathbf{d}_{\text{per}}^{(i)}\hat{s}_e(i)$. The ground state also has a permanent dipole moment, but as this is so much smaller than the other dipole moments ($d_{per'} = 1.126 \times 10^{-34}$ C m [89]) it will be neglected. We thus have two parts to our dipole operator to consider.

In the 3- and 5-level models, as we are only concerned with allowed optical transitions, transitions into and out of the intermediate singlet levels are forbidden, as are non spin conserving transitions. Thus the 3-level model has an identical transition dipole operator as for the 2-level model, and the transition dipole operator for the 5-level model is

$$\hat{\mathbf{d}}_i = 2\left(\mathbf{d}_{e_1g_1}^{(i)}\hat{s}_{1,x}^{(i)} + \mathbf{d}_{e_0g_0}^{(i)}\hat{s}_{0,x}^{(i)}\right). \tag{A.10}$$

As the intermediate singlet levels have the same electron configuration as the ground state,

$a_1'^2 a_1^2 e^2$, we assume that they will similarly have a negligible permanent dipole moment.

Electric field term

The j^{th} mode of the vacuum electric field at the position of the i^{th} NV centre is

$$\hat{\mathbf{E}}^{(j)}_{\text{vac}}(\mathbf{r}_i) = \mathbf{E}_0 \left(\exp\left(i(\mathbf{k}_j \cdot \mathbf{r}_i + \phi_j)\right) \hat{a}_j + \exp\left(-i(\mathbf{k}_j \cdot \mathbf{r}_i + \phi_j)\right) \hat{a}_j^\dagger \right) /2 \tag{A.11}$$

where $\mathbf{E}_0$ is a real vector containing the field strength and direction.

For the case of a laser operating at a frequency ω_L, direction $\mathbf{k}_L$ and possible polarizations σ, again with eq. (A.2.2), the electric field is

$$\mathbf{E}^{(j)}_{\text{laser}}(\mathbf{r}_i, t) = \mathbf{E}_0 \left(\exp\left(i(\mathbf{k}_j \cdot \mathbf{r}_i - i\omega_l t + \phi_j)\right) \alpha_j + \exp\left(-i(\mathbf{k}_j \cdot \mathbf{r}_i - i\omega_L t + \phi_j)\right) \alpha_j^* \right) /2 \tag{A.12}$$

where $j = \{\mathbf{k}_L, \sigma\}$. We also have the electric field set up by the surrounding permanent dipoles, which is

$$\hat{\mathbf{E}}_{\text{per}}(\mathbf{r}_i) = \sum_{i' \neq i} \frac{1}{4\pi\epsilon_0} \frac{3(\hat{\mathbf{d}}^{(i')}_{\text{per}} \cdot \mathbf{n}_{ii'})\mathbf{n}_{ii'} - \hat{\mathbf{d}}^{(i)}_{\text{per}}}{|\mathbf{r}_{ii'}|^3} \tag{A.13}$$

Interaction

The Hamiltonian describing the interaction of the NV centres with the environment is therefore

$$\begin{aligned} \hat{H}^{(i)}_{\text{int}} = &- \hat{\mathbf{d}}^{(i)}_{\text{per}} \cdot \hat{\mathbf{E}}^{(j)}_{\text{vac}}(\mathbf{r}_i) - \hat{\mathbf{d}}^{(i)}_{\text{per}} \cdot \mathbf{E}^{(j)}_{\text{laser}}(\mathbf{r}_i, t) - \hat{\mathbf{d}}^{(i)}_{\text{per}} \cdot \sum_{i' \neq i} \hat{\mathbf{E}}^{(i')}_{\text{per}}(\mathbf{r}_i) \\ &- \hat{\mathbf{d}}^{(i)}_{eg} \cdot \hat{\mathbf{E}}^{(j)}_{\text{vac}}(\mathbf{r}_i) - \hat{\mathbf{d}}^{(i)}_{eg} \cdot \mathbf{E}^{(j)}_{\text{laser}}(\mathbf{r}_i, t) - \hat{\mathbf{d}}^{(i)}_{eg} \cdot \sum_{j \neq i} \hat{\mathbf{E}}^{(i')}_{\text{per}}(\mathbf{r}_i) \end{aligned} \tag{A.14}$$

The first term describes the interaction of the permanent electric dipole with the vacuum field

$$\hat{H}_{\text{per-vac}} = -\sum_{i=1}^{n} \sum_j \mathbf{d}^{(i)}_{\text{per}} \cdot \mathbf{E}_0 \left(\exp\left(i(\mathbf{k}_j \cdot \mathbf{r}_i + \phi_j)\right) \hat{s}^{(i)}_e \hat{a}_j + \exp\left(-i(\mathbf{k}_j \cdot \mathbf{r}_i + \phi_j)\right) \hat{s}^{(i)}_e \hat{a}_j^\dagger \right). \tag{A.15}$$

The second term describes the interaction of the permanent electric dipole with the laser field.

$$\hat{H}_{\text{per-L}} = -\sum_{i=1}^{n}\sum_{\sigma} \mathbf{d}_{\text{per}}^{(i)} \cdot \mathbf{E}_0 \left(\exp\left(i(\mathbf{k}_j \cdot \mathbf{r}_i - i\omega_L t + \phi_j)\right) \hat{s}_e^{(i)} \alpha_{\mathbf{k}_L,\sigma} + \exp\left(-i(\mathbf{k}_j \cdot \mathbf{r}_i - i\omega_L t + \phi_j)\right) \hat{s}_e^{(i)} \alpha^*_{\mathbf{k}_L,\sigma}\right). \tag{A.16}$$

The third term describes the interaction of the permanent dipoles with the electric field of the surrounding permanent dipoles

$$\hat{H}_{\text{per-per}} = \frac{d_{\text{per}}^2}{4\pi\epsilon_0} \sum_{j\neq i} \frac{\boldsymbol{\varepsilon}^{(i)} \cdot \boldsymbol{\varepsilon}^{(j)} - 3(\boldsymbol{\varepsilon}^{(i)} \cdot \mathbf{n}_{ij})(\boldsymbol{\varepsilon}^{(j)} \cdot \mathbf{n}_{ij})}{|\mathbf{r}_{ij}|^3} |e\rangle \langle e|^{(i)} \otimes |e\rangle \langle e|^{(j)}. \tag{A.17}$$

The fourth term describes the interaction of the transition dipole with the vacuum

$$\hat{H}_{SE} = -\sum_{i=1}^{n}\sum_{j} \hbar\Omega^{(i)} \left(\exp\left(i(\mathbf{k}_j \cdot \mathbf{r}_i + \phi_j)\right) \hat{s}_x^{(i)} \hat{a}_j + \exp\left(-i(\mathbf{k}_j \cdot \mathbf{r}_i + \phi_j)\right) \hat{s}_x^{(i)} \hat{a}_j^\dagger\right) \tag{A.18}$$

where

$$\Omega^{(i)} = \begin{cases} \frac{\mathbf{d}_{e_1 g_1}^{(i)} \cdot \mathbf{E}_0}{\hbar} & \text{if the } i^{th} \text{ NV is in } m_s = \pm 1 \\ \frac{\mathbf{d}_{e_0 g_0}^{(i)} \cdot \mathbf{E}_0}{\hbar} & \text{if the } i^{th} \text{ NV is in } m_s = 0 \end{cases} \tag{A.19}$$

is the rabi frequency. The fifth term describes the interaction of the transition dipole with the laser.

$$\hat{H}_{SL} = -\sum_{i=1}^{n}\sum_{\sigma} \hbar\Omega^{(i)} \left(\exp\left(i(\mathbf{k}_j \cdot \mathbf{r}_i - \omega_L t + \phi_j)\right) \hat{s}_x^{(i)} \alpha_{\mathbf{k}_L,\sigma} + \exp\left(-i(\mathbf{k}_j \cdot \mathbf{r}_i - \omega_L t + \phi_j)\right) \hat{s}_x^{(i)} \alpha^*_{\mathbf{k}_L,\sigma}\right). \tag{A.20}$$

The final term describes the interaction of the transition dipoles with the electric field of the surrounding permanent dipoles.

$$\hat{H}_{\text{S-per}} = \frac{d_{eg} d_{\text{per}}}{4\pi\epsilon_0 n_D} \sum_{i'\neq i} \frac{\boldsymbol{\varepsilon}^{(i)} \cdot \boldsymbol{\varepsilon}^{(i')} - 3(\boldsymbol{\varepsilon}^{(i)} \cdot \mathbf{n}_{ii'})(\boldsymbol{\varepsilon}^{(i')} \cdot \mathbf{n}_{ii'})}{|\mathbf{r}_{ii'}|^3} s_x^{(i)} \otimes s_e^{(i')} \tag{A.21}$$

The parts of the Hamiltonians interacting with the laser and vacuum fields have phase terms $\exp(\pm i\mathbf{k}_j \cdot \mathbf{x}_i)$ and $\exp(\pm i\phi_j)$. This first term is a spatially dependent phase, which is dealt with in Chapter 2, and results in a metric of spatial indistinguishability. The second term is neglected, as it is constant so just results in a constant rotation. These phase terms are thus neglected in the following discussion.

A.3 Hamiltonian in the interaction picture

In general, one can move to a rotating frame by choosing $\hat{U} = \exp(-i\hat{A}t/\hbar)$, and transforming the states as $|\tilde{\psi}\rangle = \hat{U}^\dagger |\psi\rangle$. The corresponding Hamiltonian is $\tilde{H} = \hat{U}^\dagger \hat{H} \hat{U} - \hat{A}$ as

$$i\hbar \frac{d\hat{U}^\dagger |\psi\rangle}{dt} = i\hbar \hat{U}^\dagger \frac{d|\psi\rangle}{dt} + i\hbar \frac{d\hat{U}^\dagger}{dt} |\psi\rangle = \hat{U}^\dagger \hat{H} |\psi\rangle - \hat{A}\hat{U}^\dagger |\psi\rangle = (\hat{U}^\dagger \hat{H} \hat{U} - \hat{A})\hat{U}^\dagger |\psi\rangle . \quad \text{(A.22)}$$

For the Dirac/interaction frame, take $\hat{A} = \hat{H}_S + \hat{H}_E$. The rotated Hamiltonian is thus

$$\begin{aligned}
\tilde{H} &= \exp(i(\hat{H}_S + \hat{H}_E)t/\hbar)(\hat{H}_S + \hat{H}_E + \hat{H}_L + \hat{H}_{\text{per-vac}} + \hat{H}_{\text{per-L}} + \hat{H}_{\text{per-per}} + \hat{H}_{SE} + \hat{H}_{SL} + \hat{H}_{\text{S-per}}) \\
&\quad \times \exp(-i(\hat{H}_S + \hat{H}_E)t/\hbar) - \hat{H}_S - \hat{H}_E \\
&= \exp(i\hat{H}_E t/\hbar)\hat{H}_L \exp(-i\hat{H}_E t/\hbar) + \exp(i(\hat{H}_S + \hat{H}_E)t/\hbar)\hat{H}_{\text{per-vac}} \exp(-i(\hat{H}_S + \hat{H}_E)t/\hbar) \\
&\quad + \exp(i(\hat{H}_S + \hat{H}_E)t/\hbar)\hat{H}_{per-L} \exp(-i(\hat{H}_S + \hat{H}_E)t/\hbar) \\
&\quad + \exp(i(\hat{H}_S + \hat{H}_E)t/\hbar)\hat{H}_{per-per} \exp(-i(\hat{H}_S + \hat{H}_E)t/\hbar) \\
&\quad + \exp(-i(\hat{H}_S + \hat{H}_E)t/\hbar)\hat{H}_{SE} \exp(-i(\hat{H}_S + \hat{H}_E)t/\hbar) \\
&\quad + \exp(i\hat{H}_S t/\hbar)\hat{H}_{SL} \exp(-i\hat{H}_S t/\hbar) \\
&= \tilde{H}_L + \tilde{H}_{\text{per-vac}} + \tilde{H}_{\text{per-L}} + \tilde{H}_{\text{per-per}} + \tilde{H}_{SE} + \tilde{H}_{SL} + \tilde{H}_{\text{S-per}}
\end{aligned} \quad \text{(A.23)}$$

These Hamiltonians can be determined using the fact that the operators acting on the field commute with those acting on the system, and with the Baker-Campbell-Hausdorff relation,

to give, for example in the 2-level picture

$$
\begin{aligned}
\tilde{H}_L &= \sum_{\sigma} \hbar\omega_L(\alpha^*_\sigma \hat{a}_{\mathbf{k}_L,\sigma} \exp(i(\omega_L-\omega_j)t) + \alpha_\sigma \hat{a}^\dagger_{\mathbf{k}_L,\sigma} \exp(-i(\omega_L-\omega_j)t) \\
\tilde{H}_{\text{per-vac}} &= -\sum_{i=1}^{n}\sum_{j} \mathbf{d}^{(i)}_{\text{per}} \cdot \mathbf{E}_0 \left(\exp\left(-\omega_j t\right) \hat{s}^{(i)}_e \hat{a}_j + \exp\left(i\omega_j t\right) \hat{s}^{(i)}_e \hat{a}^\dagger_j\right) \\
\tilde{H}_{\text{per-L}} &= -\sum_{i=1}^{n}\sum_{\sigma} \mathbf{d}^{(i)}_{\text{per}} \cdot \mathbf{E}_0 \left(\exp\left(-i\omega_L t\right) \hat{s}^{(i)}_e \alpha_{\mathbf{k}_L,\sigma} + \exp\left(i\omega_L t\right) \hat{s}^{(i)}_e \alpha^*_{\mathbf{k}_L,\sigma}\right) \\
\tilde{H}_{SE} &= \sum_{i=1}^{n}\sum_{j} -\frac{\hbar\Omega^{(i)}}{2} \Big(\hat{s}^{(i)}_- \hat{a}_j \exp\left(-i(\omega_j+\omega_i)t\right) + \hat{s}^{(i)}_- \hat{a}^\dagger_j \exp\left(i(\omega_j-\omega_i)t\right) \\
&\quad + \hat{s}^{(i)}_+ \hat{a}_j \exp\left(-i(\omega_j-\omega_i)t\right) + \hat{s}^{(i)}_+ \hat{a}^\dagger_j \exp\left(i(\omega_j+\omega_i)t\right)\Big) \\
\tilde{H}_{SL} &= \sum_{i=1}^{n}\sum_{\sigma} -\frac{\hbar\Omega^{(i)}}{2} \Big(\hat{s}^{(i)}_- \alpha_\sigma \exp\left(-i(\omega_L+\omega_i)t\right) + \hat{s}^{(i)}_- \alpha^*_\sigma \exp\left(i(\omega_L-\omega_i)t\right) \\
&\quad + \hat{s}^{(i)}_+ \alpha_\sigma \exp\left(-i(\omega_L-\omega_i)t\right) + \hat{s}^{(i)}_+ \alpha^*_\sigma \exp\left(i(\omega_L+\omega_i)t\right)\Big) \\
\tilde{H}_{\text{per-per}} &= \frac{d^2_{\text{per}}}{4\pi\epsilon_0} \sum_{j\neq i} \frac{\boldsymbol{\varepsilon}^{(i)}\cdot\boldsymbol{\varepsilon}^{(j)} - 3(\boldsymbol{\varepsilon}^{(i)}\cdot\mathbf{n}_{ij})(\boldsymbol{\varepsilon}^{(j)}\cdot\mathbf{n}_{ij})}{|\mathbf{r}_{ij}|^3} s^{(i)}_e \otimes s^{(i')}_e \\
\tilde{H}_{\text{S-per}} &= \frac{d_{eg} d_{\text{per}}}{4\pi\epsilon_0 n_D} \sum_{i'\neq i} \frac{\boldsymbol{\varepsilon}^{(i)}\cdot\boldsymbol{\varepsilon}^{(i')} - 3(\boldsymbol{\varepsilon}^{(i)}\cdot\mathbf{n}_{ii'})(\boldsymbol{\varepsilon}^{(i')}\cdot\mathbf{n}_{ii'})}{|\mathbf{r}_{ii'}|^3} (s^{(i)}_+ \exp(i\omega_i t) + s^{(i)}_-(-i\omega_i t)) \otimes s^{(i')}_e
\end{aligned}
\tag{A.24}
$$

Using the rotating wave approximation, any terms where there is an addition of angular momentum frequencies can be discarded as they are very fast oscillating. These terms were unphysical anyway as they had excitations lost and photons destroyed together, or excitations gained and photons created together, which both violate conservation of energy. As there is summation over all ω_j, the terms with $\omega_j - \omega_i$ where the two frequencies are very close will dominate the system, so these frequencies will either be approximated as the same, or the term will be discarded. Similarly, we also discard $\omega_L + \omega_i$ terms, as these will be faster

rotating than $\omega_L + \omega_i$ terms. The Hamiltonians are thus

$$\begin{aligned}
\tilde{H}_L &= \sum_{\sigma} \hbar\omega_L \left(\alpha_\sigma^* \hat{a}_{\mathbf{k}_L,\sigma} + \alpha_\sigma \hat{a}^\dagger_{\mathbf{k}_L,\sigma}\right) \\
\tilde{H}_{SE} &= \sum_{i=1}^{n} \sum_{j} -\frac{\hbar\Omega^{(i)}}{2} \left(\hat{s}_-^{(i)} \hat{a}_j^\dagger + \hat{s}_+^{(i)} \hat{a}_j\right) \\
\tilde{H}_{SL} &= \sum_{i=1}^{n} \sum_{\sigma} -\frac{\hbar\Omega^{(i)}}{2} \left(\hat{s}_-^{(i)} \alpha_\sigma^* \exp\left(i(\omega_L - \omega_i)t\right) + \hat{s}_+^{(i)} \alpha_\sigma \exp\left(-i(\omega_L - \omega_i)t\right)\right) \\
\tilde{H}_{\text{per-per}} &= \frac{d_{\text{per}}^2}{4\pi\epsilon_0} \sum_{j\neq i} \frac{\boldsymbol{\varepsilon}^{(i)} \cdot \boldsymbol{\varepsilon}^{(j)} - 3(\boldsymbol{\varepsilon}^{(i)} \cdot \mathbf{n}_{ij})(\boldsymbol{\varepsilon}^{(j)} \cdot \mathbf{n}_{ij})}{|\mathbf{r}_{ij}|^3} s_e^{(i)} \otimes s_e^{(i')}.
\end{aligned} \tag{A.25}$$

and $\tilde{H}_{\text{per-vac}}$, $\tilde{H}_{\text{per-L}}$ and $\tilde{H}_{\text{S-per}}$ vanish, as the frequencies cannot cancel. These equations also hold for the three and 5-level models.

A.4 The Born-Markov Master equation

The derivation of the Born-Markov Master equation and its application to similar systems to this are well known. It has also been previously shown that the dipole-dipole Hamiltonian term arises due to the interaction of the system and the environment [9] [91] [42]. The typical master equation obtained, neglecting the laser part is, in the Schrödinger frame,

$$\frac{d\hat{\rho}}{dt} = -\frac{i}{\hbar}[\hat{H}_S + \hat{H}_{\text{dd}}, \hat{\rho}] - \frac{\Gamma}{2} \sum \mathcal{D}[\hat{S}]\hat{\rho} \tag{A.26}$$

where $\hat{S}$ is some jump operator, Γ is the corresponding rate, $\hat{H}_{\text{dd}}$ is the transition dipole-dipole interaction and

$$\mathcal{D}[\hat{S}]\hat{\rho} = \hat{S}^\dagger \hat{S}\hat{\rho} + \hat{\rho}\hat{S}^\dagger \hat{S} - 2\hat{S}\hat{\rho}\hat{S}^\dagger \tag{A.27}$$

In our case, the jump operators will be for collective decay and independent decay. We phenomenologically include a jump term describing dephasing, due to the coupling of the NV centres to the phononic modes in the diamond. In addition, we introduce the jump terms into and out of the I state, which could be derived through a non-optical Born-Master equation derivation. If the laser is on, that gives us an extra Hamiltonian piece. We thus

have

$$\begin{aligned}\frac{d\hat{\rho}}{dt} = &\underbrace{-\frac{i}{\hbar}[\hat{H}_S + \hat{H}_{\text{dd}} + \hat{H}_{\text{per-per}} + \hat{H}_{SL}, \hat{\rho}]}_{\text{coherent evolution}} \underbrace{-\frac{\Gamma}{2}\sum_{\sigma} P(\text{Indist.}^{(\sigma)}) \times \mathcal{D}[\hat{S}_-^{\sigma}]\hat{\rho}}_{\text{collective decay}} \\ &\underbrace{-\frac{\Gamma}{2}\sum_{i=1}^{n}\left(1 - \sum_{\sigma} P(\text{Indist.}^{(\sigma)})P(\sigma|i)\right) \times \mathcal{D}[\hat{s}_-^{(i)}]\hat{\rho}}_{\text{independent decay}} \underbrace{-\sum_{\sigma}\frac{\Gamma_{dp}^{(\sigma)}}{2}\mathcal{D}[\hat{S}_z^{\sigma}]\hat{\rho}}_{\text{global dephasing}} \underbrace{-\sum_{i=1}^{n}\frac{\Gamma_{dp}^{(\sigma)}}{2}\mathcal{D}[\hat{s}_z^{(i)}]\hat{\rho}}_{\text{local dephasing}} \\ &\underbrace{-\frac{\Gamma_{0\text{to}I}}{2}\sum_{i=1}^{n}\mathcal{D}[\hat{s}_{0\text{to}I}^{(i)}]\hat{\rho} - \frac{\Gamma_{1\text{to}I}}{2}\sum_{i=1}^{n}\mathcal{D}[\hat{s}_{1\text{to}I}^{(i)}]\hat{\rho}}_{\text{decay from the excited states into the ISC}} \underbrace{-\frac{\Gamma_{I\text{to}0}}{2}\sum_{i=1}^{n}\mathcal{D}[\hat{s}_{I\text{to}0}^{(i)}]\hat{\rho} - \frac{\Gamma_{I\text{to}1}}{2}\sum_{i=1}^{n}\mathcal{D}[\hat{s}_{I\text{to}1}^{(i)}]\hat{\rho}}_{\text{decay from the ISC into the ground states}}\end{aligned} \tag{A.28}$$

The collective operators only act collectively over the same polarization σ and domain l. Using the transition dipole operator already obtained, the transition dipole-dipole Hamiltonian is

$$\begin{aligned}\hat{H}_{\text{dd}}^{(i)} &= -\hat{\mathbf{d}}_{eg}^{(i)} \cdot \sum_{j\neq i}\hat{\mathbf{E}}_{eg}^{(j)}(\mathbf{r}_i) \\ &= \frac{d_{eg}^2 n_D}{4\pi\epsilon_0 n_D^3}\sum_{j\neq i}\frac{\boldsymbol{\varepsilon}^{(i)}\cdot\boldsymbol{\varepsilon}^{(j)} - 3(\boldsymbol{\varepsilon}^{(i)}\cdot\mathbf{n}_{ij})(\boldsymbol{\varepsilon}^{(j)}\cdot\mathbf{n}_{ij})}{|\mathbf{r}_{ij}|^3}\left(|e\rangle\langle g|^{(i)} + |g\rangle\langle e|^{(i)}\right)\otimes\left(|e\rangle\langle g|^{(j)} + |g\rangle\langle e|^{(j)}\right) \\ &= \frac{d_{eg}^2}{4\pi\epsilon_0 n_d^2}\sum_{j\neq i}\frac{\boldsymbol{\varepsilon}^{(i)}\cdot\boldsymbol{\varepsilon}^{(j)} - 3(\boldsymbol{\varepsilon}^{(i)}\cdot\mathbf{n}_{ij})(\boldsymbol{\varepsilon}^{(j)}\cdot\mathbf{n}_{ij})}{|\mathbf{r}_{ij}|^3}\left(\hat{s}_+^{(i)}\otimes\hat{s}_-^{(j)} + \hat{s}_+^{(j)}\otimes\hat{s}_-^{(i)}\right)\end{aligned} \tag{A.29}$$

To make this equation easier to simulate, it is converted from the Schrodinger frame to frame rotating at the mean angular frequency of the NV centres ω. This is done as per B.2.4, choosing $\hat{A} = \sum_{i=1}^{n}\hbar\omega\hat{s}_z^{(i)}$. The Hamiltonians thus become

$$\begin{aligned}\tilde{H}_S &= \sum_{i=1}^{n}\hbar(\omega_i - \omega)\hat{s}_z^{(i)} \\ \tilde{H}_{\text{dd}} &= \sum_{i=1}^{n}\sum_{i'=1,\neq i}^{n}\frac{3\hbar\Gamma^{(i)}}{4(n_D k)^3}\frac{\bar{d}^{(i)}\cdot\bar{d}^{(i')} - 3(\bar{d}^{(i)}\cdot\bar{n})(\bar{d}^{(i')}\cdot\bar{n})}{|\mathbf{r}_{i,j}|^3}\left(\hat{s}_+^{(i)}\hat{s}_-^{(i')} + \hat{s}_-^{(i)}\hat{s}_+^{(i')}\right)\end{aligned} \tag{A.30}$$

where the rotating wave approximation has been used in the dipole dipole Hamiltonian to eliminate $\hat{s}_+^{(i)}\hat{s}_+^{(i')}\exp(2i\omega t) + \hat{s}_-^{(i)}\hat{s}_-^{(i')}\exp(-2i\omega t)$,

$$\tilde{H}_{\text{per-per}} = -\frac{d_{\text{per}}^2}{4\pi\epsilon_0}\sum_{i'\neq i}\frac{\boldsymbol{\varepsilon}^{(i)}\cdot\boldsymbol{\varepsilon}^{(i')} - 3(\boldsymbol{\varepsilon}^{(i)}\cdot\mathbf{n}_{ij})(\boldsymbol{\varepsilon}^{(i')}\cdot\mathbf{n}_{ii'})}{|\mathbf{r}_{ii'}|^3}s_e^{(i)}\otimes s_e^{(i')} \tag{A.31}$$

and

$$\tilde{H}_{SL} = \sum_{i=1}^{n} \sum_{\sigma} -\frac{\hbar\Omega^{(i)}}{2} \left(\hat{s}_{-}^{(i)} \alpha_{\sigma}^{*} \exp\left(i(\omega_L - \omega)t\right) + \hat{s}_{+}^{(i)} \alpha_{\sigma} \exp\left(-i(\omega_L - \omega)t\right) \right). \tag{A.32}$$

In our model, we have only considered the effects of an on-resonance π polarised laser, in which case this simplifies to

$$\tilde{H}_{SL} = \sum_{i=1}^{n} -\hbar\Omega'(\bar{d}_i \cdot \bar{\epsilon}_i)\hat{s}_x^{(i)} \tag{A.33}$$

where $\Omega'(\bar{d}_i \cdot \bar{\epsilon}_i) = 2\Re(\alpha)\Omega^{(i)}$.

The Lindblad superoperator terms transform as

$$\begin{aligned} \mathcal{D}[\tilde{S}]\tilde{\rho} &= \tilde{S}^{\dagger}\tilde{S}\tilde{\rho} + \tilde{\rho}\tilde{S}^{\dagger}\tilde{S} - 2\tilde{S}\tilde{\rho}\tilde{S}^{\dagger} \\ &= \hat{S}^{\dagger}\hat{S}\tilde{\rho} + \tilde{\rho}\hat{S}^{\dagger}\hat{S} - 2\hat{S}\tilde{\rho}\hat{S}^{\dagger} \end{aligned} \tag{A.34}$$

as using $\tilde{S} = \exp(i\omega t\hat{S}_z)\hat{S}\exp(-i\omega t\hat{S}_z)$, it is clear that for all of our jump operators, they will either remain the same under rotation (for $\tilde{s}_z$ terms), or pick up a phase of $\exp(-i\omega t)$ (for $\tilde{s}_-$ terms) or $\exp(\pm i\omega t/2)$ (for $\tilde{s}_{\mathrm{ISC}}$ terms), which will cancel exactly with the phase on the $\tilde{S}\dagger$ term.

The expectation value is required for calculation of photon emission, and it is

$$\langle \tilde{S}_{+}\tilde{S}_{-} \rangle_{\tilde{\rho}} = \mathrm{Tr}(\tilde{\rho}\tilde{S}_{+}\tilde{S}_{-}) = \mathrm{Tr}(\tilde{\rho}\hat{S}_{+}\hat{S}_{-}) \tag{A.35}$$

as again the phase terms will cancel. This gives master equation which calculates $\tilde{\rho}$, but which is expressed in terms of Schrödinger operators and has expectation values calculated in terms of Schrödinger operators.

This transformation of frame is advantageous compared to the Schrödinger picture as while $\hat{H}_S$ scales with

$$\omega_i \propto \frac{1}{\Gamma - \Delta} \tag{A.36}$$

$\tilde{H}_S$ scales with

$$\omega_i - \omega \propto \frac{1}{\Gamma - \Delta} - \frac{1}{\Gamma} = \frac{\Delta}{\Gamma(\Gamma - \Delta)}. \tag{A.37}$$

$\tilde{H}_S$ is thus smaller by a factor of $\Delta/\Gamma \approx 1.5 \times 10^{-7}$.

References

[1] C. Bradac. *The properties of nitrogen-vacancy centres in nanodiamond*. Ph.D. thesis, Macquarie University (2012). URL http://hdl.handle.net/1959.14/229872.

[2] M. W. Doherty, N. B. Manson, P. Delaney, F. Jelezko, J. Wrachtrup, and L. C. Hollenberg. *The nitrogen-vacancy colour centre in diamond*. Physics Reports **528**(1), 1 (2013). URL http://linkinghub.elsevier.com/retrieve/pii/S0370157313000562.

[3] F. Jelezko, T. Gaebel, I. Popa, A. Gruber, and J. Wrachtrup. *Observation of Coherent Oscillations in a Single Electron Spin*. Physical Review Letters **92**(7), 076401 (2004). URL http://link.aps.org/doi/10.1103/PhysRevLett.92.076401.

[4] H. Aman and T. Plakhotnik. *Accuracy in the measurement of magnetic fields using nitrogen-vacancy centers in nanodiamonds*. Journal of the Optical Society of America B **33**(3), B19 (2016). URL https://www.osapublishing.org/abstract.cfm?URI=josab-33-3-B19$\backslash$nhttps://www.osapublishing.org/DirectPDFAccess/18A2CED5-D1FA-6352-ED129D14B21C7B86{_}335418/josab-33-3-B19.pdf?da=1{\&}id=335418{\&}seq=0{\&}mobile=no.

[5] J.-I. Chao, E. Perevedentseva, P.-H. Chung, K.-K. Liu, C.-Y. Cheng, C.-C. Chang, and C.-L. Cheng. *Nanometer-Sized Diamond Particle as a Probe for Biolabeling*. Biophysical Journal **93**(6), 2199 (2007). URL http://linkinghub.elsevier.com/retrieve/pii/S0006349507714753.

[6] C. Bradac, M. Johnsson, M. van Breugel, B. Baragiola, R. Martin, M. L. Juan, G. K. Brennen, and T. Volz. *Observation of room-temperature spontaneous superradiance from single diamond nanocrystals*. ArXiv: 1608.03119 pp. 1–12 (2016). 1608.03119, URL http://arxiv.org/abs/1608.03119.

[7] R. H. Dicke. *Coherence in Spontaneous Radiation Processes*. Physical Review **93**(1), 99 (1954). 1407.7336.

[8] N. Skribanowitz, I. P. Herman, J. C. MacGillivray, and M. S. Feld. *Observation of dicke superradiance in optically pumped HF gas*. Physical Review Letters **30**(8), 309 (1973).

[9] M. Gross and S. Haroche. *Superradiance: An essay on the theory of collective spontaneous emission*. Physics Reports **93**(5), 301 (1982).

[10] R. G. DeVoe and R. G. Brewer. *Observation of Superradiant and Subradiant Spontaneous Emission of Two Trapped Ions*. Phys. Rev. Lett. **76**(12), 2049 (1996). URL http://link.aps.org/doi/10.1103/PhysRevLett.76.2049.

[11] M. Scheibner, T. Schmidt, L. Worschech, A. Forchel, G. Bacher, T. Passow, and D. Hommel. *Superradiance of quantum dots*. Nature Physics **3**(2), 106 (2007).

[12] J. A. Mlynek, A. A. Abdumalikov, C. Eichler, and A. Wallraff. *Observation of Dicke superradiance for two artificial atoms in a cavity with high decay rate*. Nature Communications **5**, 5186 (2014). URL http://www.nature.com/doifinder/10.1038/ncomms6186.

[13] K. Hepp and E. H. Lieb. *On the superradiant phase transition for molecules in a quantized radiation field: the dicke maser model*. Annals of Physics **76**(2), 360 (1973).

[14] Y. Zhang, J. Lian, J. Q. Liang, G. Chen, C. Zhang, and S. Jia. *Finite-temperature Dicke phase transition of a Bose-Einstein condensate in an optical cavity*. Physical Review A - Atomic, Molecular, and Optical Physics **87**(1), 1 (2013). 1202.4125.

[15] B. M. Garraway. *The Dicke model in quantum optics: Dicke model revisited*. Philosophical Transactions of the Royal Society A: Mathematical, Physical and Engineering Sciences **369**(1939), 1137 (2011). URL http://rsta.royalsocietypublishing.org/cgi/doi/10.1098/rsta.2010.0333.

[16] J. G. Bohnet, Z. Chen, J. M. Weiner, D. Meiser, M. J. Holland, and J. K. Thompson. *A steady-state superradiant laser with less than one intracavity photon*. Nature **484**(7392), 78 (2012). URL http://dx.doi.org/10.1038/nature10920.

[17] H. W. Chan, A. T. Black, and V. Vuletic. *Observation of Collective-Emission-Induced Cooling of Atoms in an Optical Cavity*. Physical Review Letters **90**(6), 1 (2003).

[18] M. Wolke, J. Klinner, H. Keßler, and A. Hemmerich. *Cavity Cooling Below the Recoil Limit*. Science **337** (2012).

[19] L. Duan, M. D. Lukin, J. I. Cirac, and P. Zoller. *Long-distance quantum communication with atomic ensembles and linear optics*. Nature **414**, 413 (2001).

[20] A. Kuzmich, W. P. Bowen, A. D. Boozer, A. Boca, C. W. Chou, and L.-M. Duan. *Generation of nonclassical photon pairs for scalable quantum communication with atomic ensembles*. Letters to Nature **423**, 731 (2003).

[21] C. H. van der Wal, M. D. Eisaman, A. Andre, R. L. Walsworth, D. F. Phillips, A. S. Zibrov, and M. D. Lukin. *Atomic Memory for Correlated Photon States*. Science **301**, 196 (2003).

[22] A. T. Black, J. K. Thompson, and V. Vuletic. *On-Demand Superradiant Conversion of Atomic Spin Gratings into Single Photons with High Efficiency*. Physical Review Letters **95**(133601), 1 (2005).

[23] C. W. Chou, S. V. Polyakov, A. Kuzmich, and H. J. Kimble. *Single-Photon Generation from Stored Excitation in an Atomic Ensemble.* Physical Review Letters **92**(21), 1 (2004).

[24] M. H. P. M. V. Putten. *Superradiance in a Torus Magnetosphere Around a Black Hole.* Science **284**(5411), 115 (1999).

[25] N. Andersson and K. Glampedakis. *Superradiance Resonance Cavity Outside Rapidly Rotating Black Holes.* Physical Review Letters **84**(20), 4537 (2000).

[26] R. Monshouwer, M. Abrahamsson, F. van Mourik, and R. van Grondelle. *Superradiance and Exciton Delocalization in Bacterial Photosynthetic Light-Harvesting Systems.* Journal of Physics B: Atomic and Molecular Physics **101**(37), 7241 (1997).

[27] V. D. Laptev and I. V. Sokolov. *Dynamics of superradiance in a thin dielectric waveguide.* Soviet Journal of Quantum Electronics **14**(9), 1881 (1984).

[28] C. Greiner, B. Boggs, and T. W. Mossberg. *Superradiant Emission Dynamics of an Optically Thin Material Sample in a Short-Decay-Time Optical Cavity.* Physical Review Letters **85**(18), 3793 (2000).

[29] S. Slama, S. Bux, G. Krenz, C. Zimmermann, and P. W. Courteille. *Superradiant Rayleigh Scattering and Collective Atomic Recoil Lasing in a Ring Cavity.* Physical Review Letters **98**(053603), 2 (2007).

[30] A. Auffeves, D. Gerace, S. Portolan, A. Drezet, and M. Franca Santos. *Few emitters in a cavity: from cooperative emission to individualization.* New Journal of Physics **13**(093020), 1 (2011).

[31] A. Goban, C.-L. Hung, J. D. Hood, S.-P. Yu, J. A. Muniz, O. Painter, and H. J. Kimble. *Superradiance for Atoms Trapped along a Photonic Crystal Waveguide.* Physical Review Letters **115**(063601), 1 (2015).

[32] D. Meiser and M. J. Holland. *Intensity fluctuations in steady-state superradiance.* Physical Review A **063827**(81), 1 (2010).

[33] D. Meiser and M. J. Holland. *Steady-state superradiance with alkaline-earth-metal atoms.* Physical Review A **033847**(81), 1 (2010).

[34] V. V. Temnov and U. Woggon. *Superradiance and Subradiance in an Inhomogeneously Broadened Ensemble of Two-Level Systems Coupled to a Low- Q Cavity.* Physical Review Letters **95**(243602), 1 (2005).

[35] M. O Scully and A. A. Svidzinsky. *The Super of Superradiance.* Science **325**(September), 1510 (2009).

[36] A. Crubellier, D. Pavolini, A. Crubellier, D. Pavolini, and A. Crubellier. *Superradiance and subradiance : I . Interatomic interference and symmetry properties in three-level systems.* Physical Review B **18**, 3811 (1985).

[37] M. O. Scully. *Single Photon Subradiance : Quantum Control of Spontaneous Emission and Ultrafast Readout.* Physical Review Letters **115**(243602), 1 (2015).

[38] W. Guerin, M. O. Araújo, and R. Kaiser. *Subradiance in a Large Cloud of Cold Atoms.* Physical Review Letters **116**(083601), 1 (2016).

[39] T. Bienaime, N. Piovella, and R. Kaiser. *Controlled Dicke Subradiance from a Large Cloud of Two-Level Systems.* Physical Review Letters **108**(123602), 1 (2012).

[40] E. Mascarenhas, D. Gerace, M. Franca Santos, and A. Auffeves. *Cooperativity of a few quantum emitters in a single-mode cavity.* Physical Review A **063825**(88), 1 (2013).

[41] K. Lalumiere, B. C. Sanders, A. F. V. Loo, A. Fedorov, A. Wallraff, and A. Blais. *Input-output theory for waveguide QED with an ensemble of inhomogeneous atoms.* Physical Review A **88**(043806), 1 (2013).

[42] K. D. B. Higgins, S. C. Benjamin, T. M. Stace, G. J. Milburn, B. W. Lovett, and E. M. Gauger. *Superabsorption of light via quantum engineering.* Nature communications **5**, 4705 (2014). `arXiv:1306.1483v1`, URL `http://www.nature.com/ncomms/2014/140822/ncomms5705/full/ncomms5705.html`.

[43] W. Kaiser and W. L. Bond. *Nitrogen, a major impurity in common type I diamond.* Physical Review **115**(4), 857 (1959).

[44] C. Bradac, T. Gaebel, and J. R. Rabeau. *Optical Engineering of Diamond , Wiley, first ed.,* (Wiley, 2013), first ed.

[45] J. R. Rabeau, A. Stacey, A. Rabeau, S. Prawer, F. Jelezko, I. Mirza, and J. Wrachtrup. *Single nitrogen vacancy centers in chemical vapor deposited diamond nanocrystals.* Nano Letters **7**(11), 3433 (2007). `0706.2518`.

[46] J. Meijer, B. Burchard, M. Domhan, C. Wittmann, T. Gaebel, I. Popa, F. Jelezko, and J. Wrachtrup. *Generation of single color centers by focused nitrogen implantation.* Applied Physics Letters **87**(26), 1 (2005). `0505063`.

[47] D. M. Toyli, C. D. Weis, G. D. Fuchs, T. Schenkel, and D. D. Awschalom. *Chip-scale nanofabrication of single spins and spin arrays in diamond.* Nano Letters **10**(8), 3168 (2010). `1007.0240`.

[48] P. Spinicelli, A. Dreau, L. Rondin, F. Silva, J. Achard, S. Xavier, S. Bansropum, T. Debuisschert, S. Pezzagna, J. Meijer, V. Jacques, and J.-F. Roch. *Engineered arrays of nitrogen-vacancy color centers in diamond based on implantation of CN- molecules through nanoapertures.* New Journal of Physics **13**(025014), 1 (2011).

[49] A. M. Edmonds, U. F. S. D'Haenens-Johansson, R. J. Cruddace, M. E. Newton, K. M. C. Fu, C. Santori, R. G. Beausoleil, D. J. Twitchen, and M. L. Markham. *Production of oriented nitrogen-vacancy color centers in synthetic diamond.* Physical Review B - Condensed Matter and Materials Physics **86**(3), 1 (2012). `1112.5757`.

[50] T. Fukui, Y. Doi, Y. Miyamoto, H. Kato, T. Matsumoto, T. Makino, S. Yamasaki, R. Morimoto, N. Tokuda, M. Hatano, Y. Sakagawa, H. Morishita, T. Tashima, S. Miwa, Y. Suzuki, and N. Mizuochi. *Perfect selective alignment of nitrogen-vacancy centers in diamond*. Applied Physics Express **7**(055201), 1 (2014). 1403.5057.

[51] J. Michl, T. Teraji, S. Zaiser, I. Jakobi, G. Waldherr, F. Dolde, P. Neumann, M. W. Doherty, N. B. Manson, J. Isoya, and J. Wrachtrup. *Perfect alignment and preferential orientation of nitrogen-vacancy centers during chemical vapor deposition diamond growth on (111) surfaces*. Applied Physics Letters **104**(10) (2014). 1401.4106.

[52] T. Karin, S. Dunham, and K. M. Fu. *Alignment of the diamond nitrogen vacancy center by strain engineering*. Applied Physics Letters **105**(5), 2012 (2014). 1406.0041, URL http://dx.doi.org/10.1063/1.4892544.

[53] C. Kurtsiefer, S. Mayer, P. Zarda, and H. Weinfurter. *Stable solid-state source of single photons*. Physical Review Letters **85**(2), 290 (2000).

[54] J. Loubser and J. van Wyk. *Electron spin resonance in the study of diamond*. Rep. Prog. Phys. **41**, 1201 (1978).

[55] N. Bar-Gill, L. M. Pham, a. Jarmola, D. Budker, and R. L. Walsworth. *Solid-state electronic spin coherence time approaching one second*. Nature communications **4**(c), 1743 (2013). arXiv:1211.7094v2, URL http://www.ncbi.nlm.nih.gov/pubmed/23612284.

[56] T. a. Kennedy, J. S. Colton, J. E. Butler, R. C. Linares, and P. J. Doering. *Long coherence times at 300 K for nitrogen-vacancy center spins in diamond grown by chemical vapor deposition*. Applied Physics Letters **83**(2003), 4190 (2003).

[57] D. P. DiVincenzo. *The Physical Implementation of Quantum Computation*. Fortschritte der Physik **48**(9-11), 771 (2000). 0002077, URL http://arxiv.org/abs/quant-ph/0002077$\backslash$nhttp://dx.doi.org/10.1002/1521-3978(200009)48:9/11{\textless}771::AID-PROP771{\textgreater}3.0.CO;2-E.

[58] F. Jelezko, T. Gaebel, I. Popa, M. Domhan, A. Gruber, and J. Wrachtrup. *Observation of Coherent Oscillation of a Single Nuclear Spin and Realization of a Two-Qubit Conditional Quantum Gate*. Physical Review Letters **93**(13), 130501 (2004). URL http://link.aps.org/doi/10.1103/PhysRevLett.93.130501.

[59] K. Fang, V. M. Acosta, C. Santori, Z. Huang, K. M. Itoh, H. Watanabe, S. Shikata, and R. G. Beausoleil. *High-sensitivity magnetometry based on quantum beats in diamond nitrogen-vacancy centers*. Physical Review Letters **110**(13), 1 (2013). 1212.1495.

[60] K. Jensen, N. Leefer, a. Jarmola, Y. Dumeige, V. M. Acosta, P. Kehayias, B. Patton, and D. Budker. *Cavity-enhanced room-temperature magnetometry using absorption by nitrogen-vacancy centers in diamond*. ArXiv **160802**(April), 5 (2014). 1401.2438, URL http://arxiv.org/abs/1401.2438.

[61] F. Dolde, H. Fedder, M. W. Doherty, T. Nöbauer, F. Rempp, G. Balasubramanian, T. Wolf, F. Reinhard, L. C. L. Hollenberg, F. Jelezko, and J. Wrachtrup. *Electric-field sensing using single diamond spins.* Nature Physics **7**(6), 459 (2011). URL http://dx.doi.org/10.1038/nphys1969.

[62] G. Kucsko, P. C. Maurer, N. Y. Yao, M. Kubo, H. J. Noh, P. K. Lo, H. Park, and M. D. Lukin. *Nanometre-scale thermometry in a living cell.* Nature **500**(7460), 54 (2013). 1304.1068, URL http://dx.doi.org/10.1038/nature12373.

[63] A. M. Schrand, H. Huang, C. Carlson, J. J. Schlager, E. Osawa, S. M. Hussain, and L. Dai. *Are diamond nanoparticles cytotoxic?* Journal of Physical Chemistry B **111**(1), 2 (2007).

[64] D. M. Toyli, C. F. De, D. J. Christle, V. V. Dobrovitski, and D. D. Awschalom. *Fluorescence thermometry enhanced by the quantum coherence of single spins in diamond.* Proceedings of the National Academy of Sciences **110**(21), 8417 (2013).

[65] L. P. McGuinness, Y. Yan, a. Stacey, D. a. Simpson, L. T. Hall, D. Maclaurin, S. Prawer, P. Mulvaney, J. Wrachtrup, F. Caruso, R. E. Scholten, and L. C. L. Hollenberg. *Quantum measurement and orientation tracking of fluorescent nanodiamonds inside living cells.* Nature nanotechnology **6**(6), 358 (2011). URL http://dx.doi.org/10.1038/nnano.2011.64.

[66] A. Alhaddad, M. P. Adam, J. Botsoa, G. Dantelle, S. Perruchas, T. Gacoin, C. Mansuy, S. Lavielle, C. Malvy, F. Treussart, and J. R. Bertrand. *Nanodiamond as a vector for siRNA delivery to Ewing sarcoma cells.* Small **7**(21), 3087 (2011). 1106.2252.

[67] L. J. Rogers, K. D. Jahnke, M. W. Doherty, A. Dietrich, L. P. McGuinness, C. Muller, T. Teraji, H. Sumiya, J. Isoya, N. B. Manson, and F. Jelezko. *Electronic structure of the negatively charged silicon-vacancy center in diamond.* Physical Review B - Condensed Matter and Materials Physics **89**(23), 1 (2014). arXiv:1310.3131v2.

[68] M. V. Breugel. *Exploring the Silicon Vacancy Centre in CVD Grown Nanodiamond for Near-Resonant Optical Trapping.* Ph.D. thesis (2014).

[69] T. Iwasaki, F. Ishibashi, Y. Miyamoto, Y. Doi, S. Kobayashi, T. Miyazaki, K. Tahara, K. D. Jahnke, L. J. Rogers, B. Naydenov, F. Jelezko, and S. Yamasaki. *Germanium-Vacancy Single Color Centers in Diamond.* Scientific Reports **5**, 12882 (2015). URL http://dx.doi.org/10.1038/srep12882.

[70] M. L. Juan, C. Bradac, B. Besga, G. K. Brennen, G. Molina-terriza, and T. Volz. *Observation of cooperatively enhanced atomic dipole forces from NV centers in optically trapped nanodiamonds.* arXiv preprint arXiv:1511.04665 (2015). arXiv:1511.04665v1.

[71] S. Choi, J. Choi, G. Kucsko, P. C. Maurer, B. J. Shields, H. Sumiya, S. Onoda, J. Isoya, E. Demler, F. Jelezko, N. Y. Yao, and M. D. Lukin. *Depolarization dynamics in a strongly interacting solid-state spin ensemble.* arXiv:1608.05471v1 (2016). arXiv:1608.05471v1.

[72] P. Atkins and J. De Paula. *Atkins' Physical Chemistry* (W.H. Freedman and Company, 2010), 9th ed.

[73] S. M. Blinder. *Chapter 12 Molecular symmetry* pp. 1–18 (2002).

[74] J. R. Maze, A. Gali, E. Togan, Y. Chu, A. S. Trifonov, E. Kaxiras, and M. D. Lukin. *Properties of nitrogen-vacancy centers in diamond: the group theoretic approach.* New Journal of Physics **13**(2), 025025 (2011). 1010.1338, URL http://apps.webofknowledge.com.kras1.lib.keio.ac.jp/full{_}record.do?product=WOS{\&}search{_}mode=GeneralSearch{\&}qid=1{\&}SID=Q2gG7AF9ttrjIGYJLmi{\&}page=1{\&}doc=8.

[75] M. W. Doherty, N. B. Manson, P. Delaney, and L. C. Hollenberg. *The negatively charged nitrogen-vacancy centre in diamond: the electronic solution.* New Journal of Physics **13**(2), 025019 (2011). 1008.5224, URL http://stacks.iop.org/1367-2630/13/i=2/a=025019?key=crossref.9dc849f93a4bc63bf89c15afa6abaf62.

[76] Y. Chu and M. D. Lukin. *Quantum optics with nitrogen-vacancy centers in diamond.* arXiv: 1504.05990 (2015). 1504.05990, URL http://arxiv.org/abs/1504.05990.

[77] N. B. Manson and R. L. McMurtrie. *Issues concerning the nitrogen-vacancy center in diamond.* Journal of Luminescence **127**(1), 98 (2007).

[78] L. J. Rogers, R. L. McMurtrie, M. J. Sellars, and N. B. Manson. *Time-averaging within the excited state of the nitrogen-vacancy centre in diamond.* New Journal of Physics **11**(6), 063007 (2009). 0902.2256, URL http://stacks.iop.org/1367-2630/11/i=6/a=063007.

[79] G. Davies and M. F. Hamer. *Optical Studies of the 1.945 eV Vibronic Band in Diamond.* Proceedings of the Royal Society of London. Series A, Mathematical and Physical Sciences **348**(1653), 285 (1976).

[80] V. M. Huxter, T. a. a. Oliver, D. Budker, and G. R. Fleming. *Vibrational and electronic dynamics of nitrogen–vacancy centres in diamond revealed by two-dimensional ultrafast spectroscopy.* Nature Physics **9**(10), 1 (2013). URL http://dx.doi.org/10.1038/nphys2753$\backslash$npapers2://publication/doi/10.1038/nphys2753.

[81] V. M. Acosta, A. Jarmola, E. Bauch, and D. Budker. *Optical properties of the nitrogen-vacancy singlet levels in diamond.* Physical Review B **82**, 1 (2010).

[82] M. Goldman, A. Sipahigil, M. W. Doherty, N. Yao, S. Bennett, M. Markham, D. Twitchen, N. B. Manson, A. Kubanek, and M. D. Lukin. *Phonon-Induced Population Dynamics and Intersystem Crossing in Nitrogen-Vacancy Centers.* Physical Review Letters **114**(14), 145502 (2015). URL http://link.aps.org/doi/10.1103/PhysRevLett.114.145502.

[83] N. B. Manson, J. P. Harrison, and M. J. Sellars. *Nitrogen-vacancy center in diamond: Model of the electronic structure and associated dynamics.* Physical Review B **74**(10), 104303 (2006). URL http://link.aps.org/doi/10.1103/PhysRevB.74.104303.

[84] L. Robledo, H. Bernien, T. van der Sar, and R. Hanson. *Spin dynamics in the optical cycle of single nitrogen-vacancy centres in diamond.* New Journal of Physics **13**(025013), 1 (2011).

[85] E. Wigner. *Gruppentheorie und ihre Anwendung auf die Quantenmechanik der Atomspektren* (Springer Fachmedien Wiesbaden GmbH, 1931).

[86] I. Wolfram Research. *Mathematica* (Wolfram Research, Inc., Champaign, Illinois, 2015), version 10 ed.

[87] P. Tamarat, N. B. Manson, J. P. Harrison, R. L. McMurtrie, A. P. Nizovtsev, C. Santori, R. G. Beausoleil, P. Neumann, T. Gaebel, F. Jelezko, P. R. Hemmer, and J. Wrachtrup. *Spin-flip and spin-conserving optical transitions of the nitrogen-vacancy centre in diamond.* New Journal of Physics **10**(2008), 1 (2008).

[88] P. Tamarat, T. Gaebel, J. R. Rabeau, M. Khan, A. D. Greentree, H. Wilson, L. C. L. Hollenberg, S. Prawer, P. Hemmer, F. Jelezko, and J. Wrachtrup. *Stark shift control of single optical centers in diamond.* Physical Review Letters **97**(8), 1 (2006). 0607170.

[89] E. Van Oort and M. Glasbeek. *Electric-field-induced modulation of spin echoes of N-V centers in diamond.* Chemical Physics Letters **168**(6), 529 (1990).

[90] F. A. Inam, T. Gaebel, C. Bradac, L. Stewart, M. J. Withford, J. M. Dawes, J. R. Rabeau, and M. J. Steel. *Modification of spontaneous emission from nanodiamond colour centres on a structured surface.* New Journal of Physics **13**, 1 (2011).

[91] G. K. Brennen. *Quantum Logic Gates with Neutral Atoms in an Optical Lattice.* Ph.D. thesis, University of New Mexico (2001).

[92] A. Albrecht, A. Retzker, F. Jelezko, and M. B. Plenio. *Coupling of nitrogen vacancy centres in nanodiamonds by means of phonons.* New Journal of Physics **15**(8), 083014 (2013). 1304.2192, URL http://stacks.iop.org/1367-2630/15/i=8/a=083014?key=crossref.853c4fa547d78f4b5e11132515117be9.

[93] R. P. Roberts. *Quantum-optical trapping of nanodiamonds containing NV centres By.* Ph.D. thesis (2015).

[94] K. Borsuk. *Drei Sätze über die n-dimensionale euklidische Sphäre.* Fundamenta Mathematicae **20** (1933).

[95] E. Fermi. *Quantum Theory of Radiation.* Reviews of Modern Physics **4**, 88 (1932).

[96] D. Buchholz and J. Yngvason. *There Are No Causality Problems for Fermi's Two-Atom System.* Physical Review Letters **73**(5), 613 (1994).

[97] P. W. Milonni and P. L. Knight. *Retardation in the resonant interaction of two identical atoms.* Physical Review A **10**(4), 1096 (1974).

[98] R. Brewer. *Two-ion superradiance theory.* Physical review. A **52**(4), 2965 (1995). URL http://www.ncbi.nlm.nih.gov/pubmed/9920643.

[99] E. Ressayre and A. Tallet. *Quantum Theory for Superradiance.* Physical Review A **15**(6), 2410 (1977).

[100] G. D. Fuchs, V. V. Dobrovitski, R. Hanson, A. Batra, C. D. Weis, T. Schenkel, and D. D. Awschalom. *Excited-State Spectroscopy Using Single Spin Manipulation in Diamond* **117601**(September), 19 (2008).

[101] C. Navarrete-Benlloch. *Open systems dynamics: Simulating master equations in the computer.* arXiv preprint arXiv: 1504.05266v2 pp. 1–18 (2015). 1504.05266, URL http://arxiv.org/abs/1504.05266.

[102] C. D. Weis, A. Schuh, A. Batra, A. Persaud, I. W. Rangelow, J. Bokor, C. C. Lo, S. Cabrini, G. D. Fuchs, R. Hanson, D. D. Awschalom, and T. Schenkel. *Single atom doping for quantum device development in diamond and silicon Single atom doping for quantum device development in diamond.* Journal of Vacuum Science and Technology B **26**(2596), 1 (2008).

[103] S. Pezzagna, D. Wildanger, P. Mazarov, A. D. Wieck, Y. Sarov, I. Rangelow, B. Naydenov, F. Jelezko, S. W. Hell, and J. Meijer. *Nanoscale Engineering and Optical Addressing of Single Spins in Diamond.* Small **6**(19), 2117 (2010).

[104] B. Naydenov, V. Richter, J. Beck, M. Steiner, P. Neumann, J. Achard, F. Jelezko, J. Wrachtrup, R. Kalish, B. Naydenov, V. Richter, J. Beck, M. Steiner, P. Neumann, G. Balasubramanian, J. Achard, F. Jelezko, J. Wrachtrup, and R. Kalish. *Enhanced generation of single optically active spins in diamond by ion implantation.* Applied Physics Letters **96**(163108), 8 (2010).

[105] B. J. M. Hausmann, T. M. Babinec, J. T. Choy, J. S. Hodges, S. Hong, I. Bulu, A. Yacoby, M. D. Lukin, and M. Loncar. *Single-color centers implanted in diamond nanostructures.* New Journal of Physics **12**(045004), 1 (2011).

[106] J. Schwartz, P. Michaelides, C. D. Weis, and T. Schenkel. *In situ optimization of co-implantation and substrate temperature conditions for nitrogen- vacancy center formation in single-crystal diamonds.* New Journal of Physics **13**(035022), 1 (2011).

[107] S. Pezzagna, D. Rogalla, I. Jakobi, F. Dolde, B. Naydenov, J. Wrachtrup, F. Jelezko, C. Trautmann, and J. Meijer. *Creation of colour centres in diamond by collimated ion-implantation through nano-channels in mica.* Physica Status Solidi (A) Applications and Materials Science **208**(9), 2017 (2011).

[108] T. Miyazaki, Y. Miyamoto, T. Makino, H. Kato, S. Yamasaki, T. Fukui, Y. Doi, N. Tokuda, M. Hatano, and N. Mizuochi. *Atomistic mechanism of perfect alignment of nitrogen-vacancy centers in diamond.* Applied Physics Letters **105**(26), 2012 (2014). 1409.2573, URL http://dx.doi.org/10.1063/1.4904988.